Modeling nanoscale charge measurements

Daniel Heile, Reinhard Olbrich, Michael Reichling, and Philipp Rahe*
Fachbereich Mathematik/Informatik/Physik, Universität Osnabrück, Barbarastraße 7, 49076 Osnabrück, Germany

(Received 23 November 2022; revised 4 June 2023; accepted 5 June 2023; published 15 August 2023)

The quantitative measurement of charges at the nanoscale yields important insights into fundamental physical, chemical, or biological processes. In principle, charges can be probed by the sharp tip of a dynamic atomic force microscope, however, quantitative measurements are still a challenge as a large number of parameters and effects contribute to the measured signal. Here, we introduce the fundamental framework for charge force microscopy (CFM) and investigate charges located in, on, or above the surface of a dielectric substrate supported by a metal electrode. We present a comprehensive analysis of CFM signal generation and, in particular, unravel the dependency of the CFM signal on the probe oscillation amplitude, on system parameters such as the substrate dielectric constant or the tip geometry, and on the vertical and lateral position of charges. Most importantly, we untangle the influence from nearby charges when quantifying the magnitude of a central charge of interest in presence of many surrounding charges. We find that charge quantification from regular imaging bears many ambiguities, while mapping the CFM signal perpendicular to the sample surface allows to untangle many signal contributions. Thus, by accounting for measurement parameters and nonlocal influences, quantitative measurements are possible with CFM.

DOI: 10.1103/PhysRevB.108.085420

I. INTRODUCTION

Measuring and controlling the charge state of nanoscale objects is paramount in a large number of research fields including catalysis, organic and molecular electronics, quantum sensors, or energy storage [1–3]. A *change* in the charge state of a nano-object can well be detected by dynamic techniques of measuring forces between a fine tip and the object of interest with a sensitivity down to single electrons [4–8] and atomic-scale resolution has been achieved [9,10]. In contrast, the *quantification* of the static charge magnitude accumulated in a nano-object is still most challenging [11]. In addition to the long-range character of the electrostatic force, the electric potential distribution governing the tip-surface interaction critically depends on the nanoscale size and shape of the tip that can hardly be produced or characterized with the desired precision.

Here, we address fundamental aspects for an experimental quantification of charges below, on, or above the surface of an electrically insulating substrate. Charge measurements are implemented using the technology of frequency-modulated (FM) closed-loop (CL) Kelvin probe force microscopy (KPFM), a nanoscale imaging technique that is rooted in the measurement of the work function difference between tip and sample for metal and semiconductor surfaces [12–14]. The KPFM measurement signal is generally referred to as the contact potential difference (CPD) [15] and the spatial resolution power is reflected by introducing the concept of both a *local* work function [16] as well as a *local* contact potential difference [15]. The central measurement parameter in KPFM is the bias voltage V_{bias} applied between the electrically conducting tip and the conducting sample.

In this work, we investigate charges near a dielectric support and V_{bias} refers to the voltage applied between the tip and a metallic counter electrode. The primary outcome of a charge measurement experiment is the force-minimizing bias voltage $V_{\mathrm{bias}}^{\mathrm{min}}$ that is the response in the FM-CL force measurement. For our analysis, we build on previous work where a formalism was outlined allowing a simple representation of $V_{\mathrm{bias}}^{\mathrm{min}}$ in terms of the charges q_i and the weighted average of the second derivatives of the tip-surface electric potential Φ_{void} at the charge positions $\vec{r}_i$ as well as the weighted average of the second derivative of the void capacitance C_{void} along the tip-sampling path [17]. Together, these averages provide a weight function $W_{\mathrm{q}}(\vec{r}_i)$ [18], which determines the contribution of the respective charge to the $V_{\mathrm{bias}}^{\mathrm{min}}$ voltage signal. For a valid interpretation of measurement data, the contact potential difference between tip and sample support V_{CPD} that is part of the measured signal $V_{\mathrm{bias}}^{\mathrm{min}}$ has to be taken into account. Measuring $V_{\mathrm{bias}}^{\mathrm{min}}$ is further on referred to as the method of charge force microscopy (CFM).

Here, we investigate by extensive modeling how a static charge magnitude can be measured by monitoring the CFM voltage $V_{\mathrm{bias}}^{\mathrm{min}}$ when approaching the tip to the surface in the vicinity of the charge. In particular, we use three different geometric models for the tip and investigate $V_{\mathrm{bias}}^{\mathrm{min}}$ for different oscillation amplitudes, different dielectric properties of the substrate, different charge positions, and different charge distributions around a central charge of interest. We find that the CFM voltage acquired as a function of the tip-sample distance z_{ts} is key to charge quantification, while commonly used imaging bears many ambiguities.

The paper is organized as follows: In Sec. II we review the physical model, introduce three tip geometries that are used

*prahe@uos.de

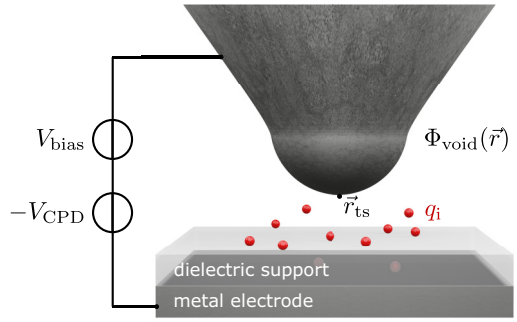

FIG. 1. Geometry of a tip in proximity of a dielectric support fixed on a metallic counter electrode. Point charges q_i (red spheres) are located between tip and metal electrode. The void (charge-free) tip-sample capacitor is physically described by the electrostatic potential $\Phi_{\mathrm{void}}(\vec{r})$. An external voltage V_{bias} is applied between tip and metal counter electrode, while a voltage $-V_{\mathrm{CPD}}$ is generated upon electrical contact between the two metals. The vector $\vec{r}_{\mathrm{ts}} = [x_{\mathrm{ts}}, y_{\mathrm{ts}}, z_{\mathrm{ts}}]$ describes the momentary tip position with z_{ts} being the tip-sample distance.

for the simulations, and discuss the electrostatic quantities relevant for $W_{\mathrm{q}}(\vec{r}_i)$. The influence of the probe oscillation amplitude A, the impact of the dielectric constant ϵ_{s} of the substrate, and effects of the tip geometry on the charge measurement are analysed in Sec. III. In Sec. IV, we investigate the influence of the lateral and vertical positions of a single point charge on the distance-dependent CFM signal. Section V addresses charge quantification by introducing a methodology to retrieve the charge of a central pointlike object in the vicinity of secondary charges from $V_{\mathrm{bias}}^{\mathrm{min}}$ data. We conclude in Sec. VI with a summary of major results and propositions for a successful implementation of CFM measurements.

II. ELECTROSTATIC MODEL AND CFM FUNDAMENTALS

A model representation of the tip-sample geometry is shown in Figs. 1 and 2. The system is described in the sample coordinate system $\vec{r} = (x, y, z)$ where the tip is positioned at $\vec{r}_{\mathrm{ts}} = [x_{\mathrm{ts}}, y_{\mathrm{ts}}, z_{\mathrm{ts}}]$. Following previously outlined definitions [19], the z axis is perpendicular to the substrate surface, its origin $z = 0$ is at the surface, and z_{ts} is the closest tip-sample distance during one tip oscillation cycle. The tip is brought into close proximity to the surface of a thick dielectric support with relative permittivity ϵ_{s} that is fixed on a metal plate acting as the counter electrode with respect to the tip. Charges q_i placed at positions $\vec{r}_i$ in, on, or above the dielectric support represent point charges or charged nanoscale objects that are subject of investigation. The model works under the assumption that the tip is an ideal metal free of excess charge. The surface of the tip is assumed to be smooth as well as bare of atomic structure and the tip can be described by a macroscopic model [20]. A variable voltage V_{bias} is applied between tip and counter electrode, while the voltage $-V_{\mathrm{CPD}}$ appears upon establishing electrical contact between tip and counter electrode.

The electrostatic force F_{el} acting on the probing tip is the central quantity for charge quantification as it is fundamental for determining the voltage $V_{\mathrm{bias}}^{\mathrm{min}}$. This force can be calculated from the electrostatic energy of the full physical setup, whereby the tip-sample system, the point charges, as well as the external bias supply have to be taken into account. For the tip-sample system, the electrostatic energy can be calculated from solving the electrostatic problem for the given tip and sample geometry including the point charges and the dielectric support. Additionally, the work performed by the external bias supply has to be taken into account in the energy calculation. A solution of the more general electrostatic problem, namely, a system containing an arbitrary number of metal objects and point charges with an external battery, has been given before [21]. For our purpose, this analysis has been reduced to the case of two metals, one representing the tip and the second the counter electrode, as well as N point charges [17]. This allows to write the total electrostatic energy U_{el} as a sum of four contributions [22], namely,

$$U_{\mathrm{el}} = U_{\mathrm{C}} + U_{\mathrm{q\text{-}C}} + U_{\mathrm{q\text{-}q}} + U_{\mathrm{im}}. \tag{1}$$

The first term U_{C} describes the capacitive interaction between tip and metal electrode with an interjacent dielectric medium. This energy is independent of the point charges, but establishes the quadratical dependence of the interaction force on V_{bias}. The quantity governing this contribution is the void capacitance $C_{\mathrm{void}}(\vec{r}_{\mathrm{ts}})$, where $\vec{r}_{\mathrm{ts}}$ is the momentary tip position. By *void* we denote all quantities of the charge-free system.

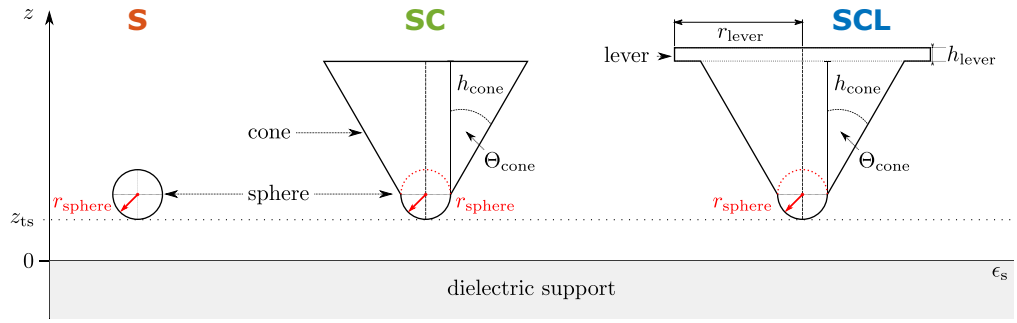

FIG. 2. Cross sections of the three model tips and system geometries: sphere (S), half-sphere and cone (SC), as well as half-sphere and cone with lever (SCL). The sphere is parametrized by the radius r_{sphere}, the cone by the cone height h_{cone} and half opening angle Θ_{cone}, and the lever by the radius r_{lever} and the thickness h_{lever}. The tip-sample distance z_{ts} (marked by the dotted line) is defined as the distance between the surface of the dielectric support with relative permittivity ϵ_{s} and the point of the tip closest to the surface.

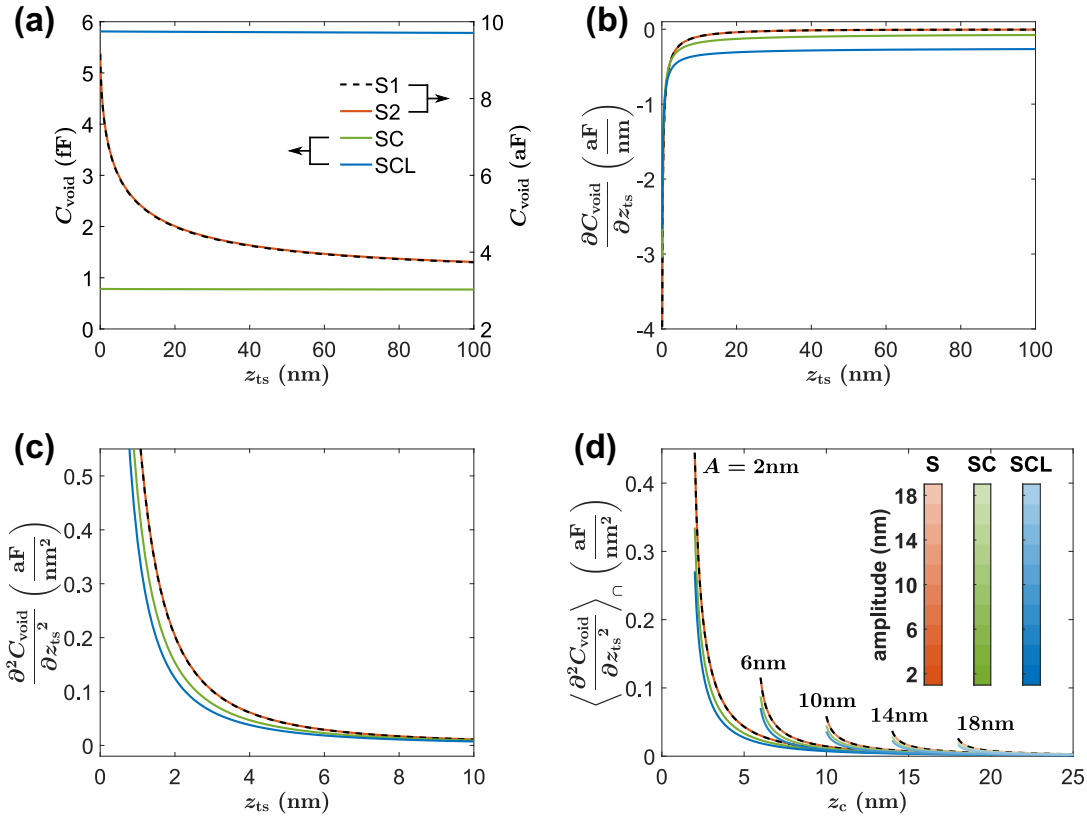

FIG. 3. (a) Capacitance C_{void} as well as (b) first, (c) second, and (d) cap-averaged second derivative of the capacitance for tip models S, SC, and SCL. Data in (a)–(c) are plotted with respect to the tip-sample distance z_{ts}, while data in (d) are plotted with respect to the tip oscillation center position z_{c} [19] for oscillation amplitudes A in the range of 2 to 18 nm. Tip model parameters listed in Table I and $\epsilon_{\text{s}} = 24$ are used in the calculation. For geometry S, results calculated by the analytical [25] (S1) and numerical [24] (S2) codes are depicted by black dashed and straight red lines, respectively. Results for the SC and SCL models are depicted in green and blue, respectively.

The system is modeled by two metals representing the tip and the counter electrode with the potential difference V between these two metals. Further analysis shows that the capacitive term is an important experimental parameter but not directly relevant for charge measurements. Instead, the second energy contribution $U_{\text{q-C}}$ is central for charge quantification as this term describes the energy required to bring the point charges q_i into the capacitor at positions $\vec{r}_i$. In particular, the energy for each point charge i can be expressed by a product between the point-charge magnitude q_i and the electrostatic potential of the point-charge free capacitor $\Phi_{\text{void}}(\vec{r}_{\text{ts}}, \vec{r}_i)$ for a given tip position $\vec{r}_{\text{ts}}$ and at the position of the charge $\vec{r}_i$. For the ease of calculation, the electrostatic potential is normalized by the potential difference V, resulting in the normalized electrostatic potential $\hat{\Phi}_{\text{void}} = \Phi_{\text{void}}/V$. The Coulomb interaction between the point charges is described by the third term $U_{\text{q-q}}$. Descriptively, this is the energy required to introduce each point charge into the field of the other point charges. The fourth term U_{im} describes the energy contribution of all image charges at the metal surfaces that are generated by the point charges.

Using Eq. (1), the electrostatic force F_{el} is calculated from the negative derivative of the total energy U_{el} with respect to the tip-sample distance z_{ts}. The restriction of the derivative to the coordinate z_{ts} is justified by the constraint of the probe solely oscillating along z_{ts} without any other degree of freedom. The electrostatic force consists of four terms, namely [22],

$$F_{\text{el}}(z_{\text{ts}}, V) = \frac{1}{2}\frac{\partial C_{\text{void}}}{\partial z_{\text{ts}}}V^2 - \sum_{i=1}^{N} q_i \frac{\partial \hat{\Phi}_{\text{void}}(\vec{r}_i)}{\partial z_{\text{ts}}}V - \frac{\partial U_{\text{q-q}}}{\partial z_{\text{ts}}} - \frac{1}{2}\sum_{i=1}^{N} q_i \frac{\partial \Phi_{\text{im}}(\vec{r}_i)}{\partial z_{\text{ts}}}. \tag{2}$$

The first term follows from the capacitive contribution to the electrostatic force and is always attractive as $\frac{\partial C_{\text{void}}}{\partial z_{\text{ts}}} < 0$ as shown in Fig. 3(b). This term enables the measurement of the voltage V_{CPD} in KPFM experiments [14]. The second term is the key contribution to CFM measurements as it describes the force acting between the charges and the metal objects. The third term vanishes ($\frac{\partial U_{\text{q-q}}}{\partial z_{\text{ts}}} = 0$) as electrostatic forces and counterforces compensate each other in an ensemble of charges held at fixed positions. The fourth term is caused by charge redistribution on the metal surfaces, commonly referred to as the image charge. The related potential Φ_{im} is independent of the potential difference V and, therefore, does not contribute to $V_{\text{bias}}^{\text{min}}$ as the force minimizing bias voltage is derived from the derivation with respect to V.

The basic principle of CFM is the variation of V_{bias} to find the point of minimum attractive force at $V_{\text{bias}}^{\text{min}}$ where the repulsive charge-dependent force best counteracts the

TABLE I. Parameters for the tip models S, SC, and SCL utilized for all calculations unless otherwise noted.

Model	r_{sphere} (nm)	Θ_{cone} (deg)	h_{cone} (μm)	r_{lever} (μm)	h_{lever} (μm)
S	30.0				
SC	30.0	23.3	12.5		
SCL	30.0	23.3	12.5	34.6	4.0

attractive capacitive force under conditions of a dynamic measurement. For a measurement with frequency modulation and closed-loop force minimization, the total potential difference V between tip and sample is represented as

$$V = V_{\text{bias}} - V_{\text{CPD}} + V_{\text{el}} \cos(2\pi f_{\text{el}} t) \tag{3}$$

with the contact potential difference V_{CPD}, the bias voltage V_{bias}, and a bias modulation with amplitude V_{el} and frequency f_{el}. The negative sign for V_{CPD} is used to follow the common convention in the KPFM literature [15]. As a result of the bias modulation, the electrostatic force measured by the tip is a modulated signal with spectral components at f_{el} and $2f_{\text{el}}$, namely [22],

$$F_{\text{el}} = F_{\text{el,a}} + F_{\text{el,b}} \cos(2\pi f_{\text{el}} t) + F_{\text{el,c}} \cos(2\pi 2 f_{\text{el}} t). \tag{4}$$

Terms $F_{\text{el,a}}$ and $F_{\text{el,c}}$ are given in Ref. [22]. The term

$$F_{\text{el,b}} = V_{\text{el}} \left(\frac{\partial C_{\text{void}}}{\partial z_{\text{ts}}} (V_{\text{bias}} - V_{\text{CPD}}) - \sum_{i=1}^{N} q_i \frac{\partial \hat{\Phi}_{\text{void}}(\vec{r}_i)}{\partial z_{\text{ts}}} \right) \tag{5}$$

is relevant for CFM as this component contains the full information on the charge distribution. It can be shown [22] that the dynamic measurement with FM detection yields a signal proportional to the cycle-averaged force gradient

$$\left\langle \frac{\partial F_{\text{el,b}}}{\partial z_{\text{ts}}} \right\rangle_{\cap} = V_{\text{el}} \left(\left\langle \frac{\partial^2 C_{\text{void}}}{\partial z_{\text{ts}}^2} \right\rangle_{\cap} (V_{\text{bias}} - V_{\text{CPD}}) - \sum_{i=1}^{N} q_i \left\langle \frac{\partial^2 \hat{\Phi}_{\text{void}}(\vec{r}_i)}{\partial z_{\text{ts}}^2} \right\rangle_{\cap} \right), \tag{6}$$

whereby $\langle \ldots \rangle_{\cap}$ denotes the cap-weighted average function [23]

$$\langle f \rangle_{\cap}(z_{\text{c}}) = \frac{2}{\pi A^2} \int_{-A}^{A} f(z_{\text{c}} + z) \sqrt{A^2 - z^2}\, dz \tag{7}$$

with the tip oscillation center position z_{c} and the oscillation amplitude A as introduced in Ref. [19]. The CFM signal voltage $V_{\text{bias}}^{\text{min}}$ directly follows from setting Eq. (6) to be equal

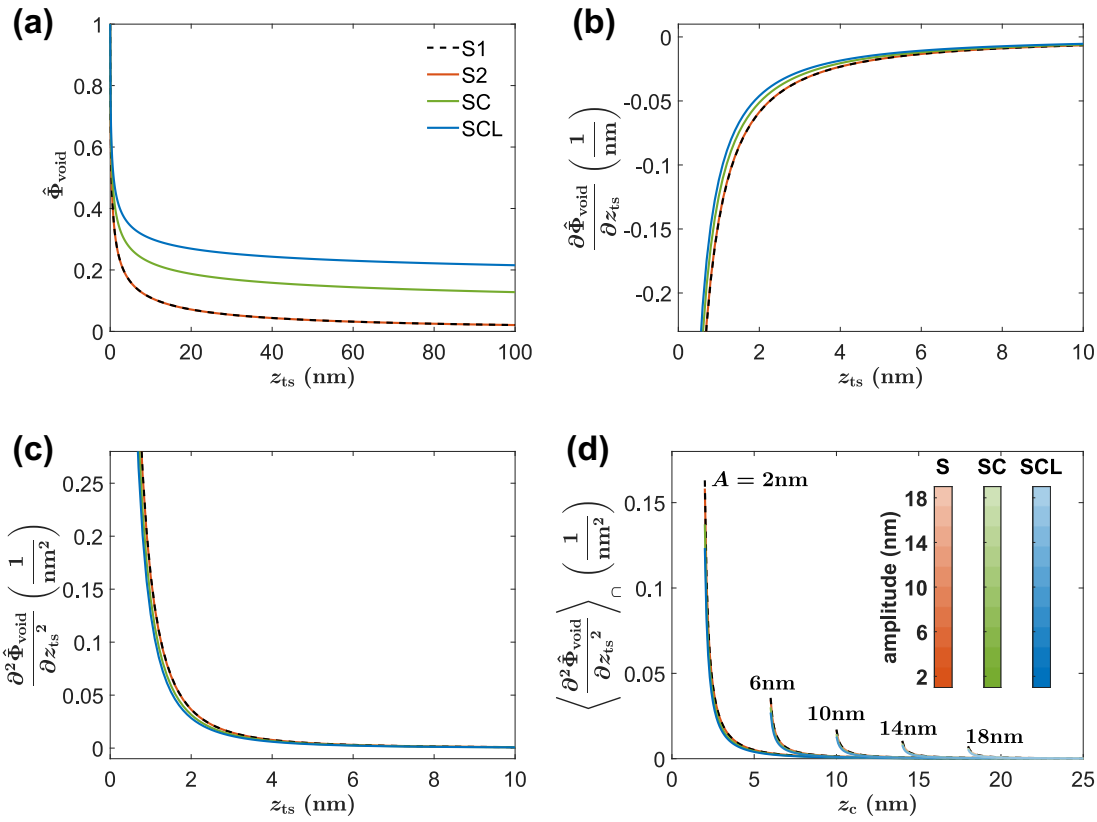

FIG. 4. (a) Normalized electrostatic potential $\hat{\Phi}_{\text{void}}$ as well as (b) first, (c) second, and (d) cap-averaged second derivative of the normalized electrostatic potential evaluated at position $\vec{r}_0 = [0, 0, 0]$ for tip models S, SC, and SCL. Data in (a)–(c) are plotted with respect to the tip-sample distance z_{ts}, while data in (d) are plotted with respect to the tip oscillation center position z_{c} [19] for oscillation amplitudes A in the range of 2 to 18 nm. Tip-model parameters listed in Table I and $\epsilon_{\text{s}} = 24$ are used in the calculation. For geometry S, results calculated by the analytical [25] (S1) and numerical [24] (S2) codes are depicted by black dashed and straight red lines, respectively. Results for the SC and SCL models are depicted in green and blue, respectively.

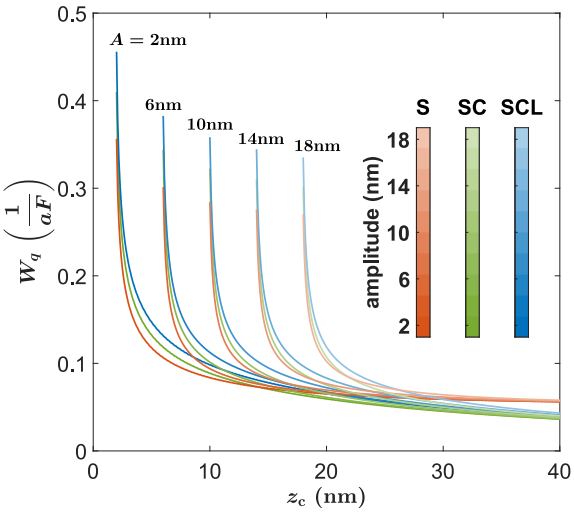

FIG. 5. Weight function W_q as a function of the tip oscillation center position z_c [19] calculated at the position $\vec{r}_0 = [0, 0, 0]$ for models S, SC, and SCL as well as for amplitudes A in the range from 2 to 18 nm. Increasing amplitudes are represented by successively tinted colors (colors with increased lightness) as indicated by the color bars.

to zero. Technically, this is usually realized by a feedback loop adjusting V_{bias} to the point of vanishing signal $\langle \frac{\partial F_{\text{el,b}}}{\partial z_{\text{ts}}} \rangle_{\cap}$ with respect to V_{bias}; this signal can be measured from the f_{el} component in the frequency-shift signal Δf. Narrow-band and phase-sensitive detection of this component yields a high signal-to-noise ratio for measuring $V_{\text{bias}}^{\text{min}}$ as the small voltage modulation amplitude V_{el} effectively produces a differentiation with respect to V_{bias}. The CFM signal then reads as [17]

$$V_{\text{bias}}^{\text{min}} = V_{\text{CPD}} + \sum_{i=0}^{N} q_i \frac{\left\langle \frac{\partial^2 \hat{\Phi}_{\text{void}}(\vec{r}_i)}{\partial z_{\text{ts}}^2} \right\rangle_{\cap}}{\left\langle \frac{\partial^2 C_{\text{void}}}{\partial z_{\text{ts}}^2} \right\rangle_{\cap}}. \tag{8}$$

This equation can be written in a compact form by introducing the weight function for charges $W_{\text{q}}(\vec{r}_i)$ [18] evaluated at the charge position $\vec{r}_i$:

$$V_{\text{bias}}^{\text{min}} = V_{\text{CPD}} + \sum_{i=0}^{N} q_i W_{\text{q}}(\vec{r}_i) \;\text{ with }\; W_{\text{q}}(\vec{r}_i) = \frac{\left\langle \frac{\partial^2 \hat{\Phi}_{\text{void}}(\vec{r}_i)}{\partial z_{\text{ts}}^2} \right\rangle_{\cap}}{\left\langle \frac{\partial^2 C_{\text{void}}}{\partial z_{\text{ts}}^2} \right\rangle_{\cap}}. \tag{9}$$

Two electrostatic quantities contribute to the weight function W_{q}, namely, the normalized electrostatic potential $\hat{\Phi}_{\text{void}}$ evaluated at charge positions $\vec{r}_i$ and the capacitance C_{void}, both for the given tip position $\vec{r}_{\text{ts}}$. To evaluate these quantities, the tip-sample system has to be defined in all details, namely, the tip geometry (formally described by a set of parameters $\{p_{\text{tip}}\}$), the tip position $\vec{r}_{\text{ts}} = [x_{\text{ts}}, y_{\text{ts}}, z_{\text{ts}}]$, the dielectric constant ϵ_{s} of the dielectric support, and the tip oscillation amplitude A via the cap-average $\langle \ldots \rangle_{\cap}$. The vertical tip position of the averaged quantities is parametrized by either the tip oscillation center position z_{c} or the position of the lower turning point during the oscillation cycle $z_{\text{ts}}^{\text{min}} = z_{\text{c}} - A$ [19]. Taking

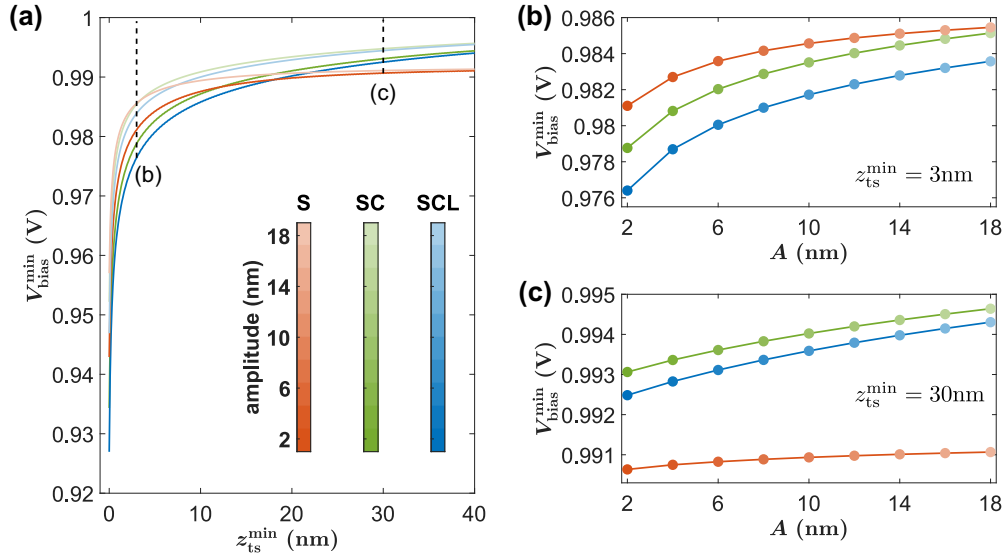

FIG. 6. $V_{\text{bias}}^{\text{min}}$ voltage calculated for models S, SC, and SCL as a function of (a) $z_{\text{ts}}^{\text{min}}$ for amplitudes A in the range from 2 to 18 nm as well as (b), (c) as a function of the oscillation amplitude A at fixed minimum tip-sample distances of (b) 3 nm and (c) 30 nm. Equation (8) is evaluated at $\vec{r}_0 = [0, 0, 0]$ for a single point charge $q = -e$ (with the elementary charge $e > 0$) located at this position. Tip-model parameters listed in Table I, $\epsilon_{\text{s}} = 24$, and $V_{\text{CPD}} = 1$ V are used in the calculation. Increasing amplitudes are represented by successively tinted colors [see color bars in (a)]. For clarity, only the $V_{\text{bias}}^{\text{min}}$ curves for the smallest and largest amplitudes are depicted in (a).

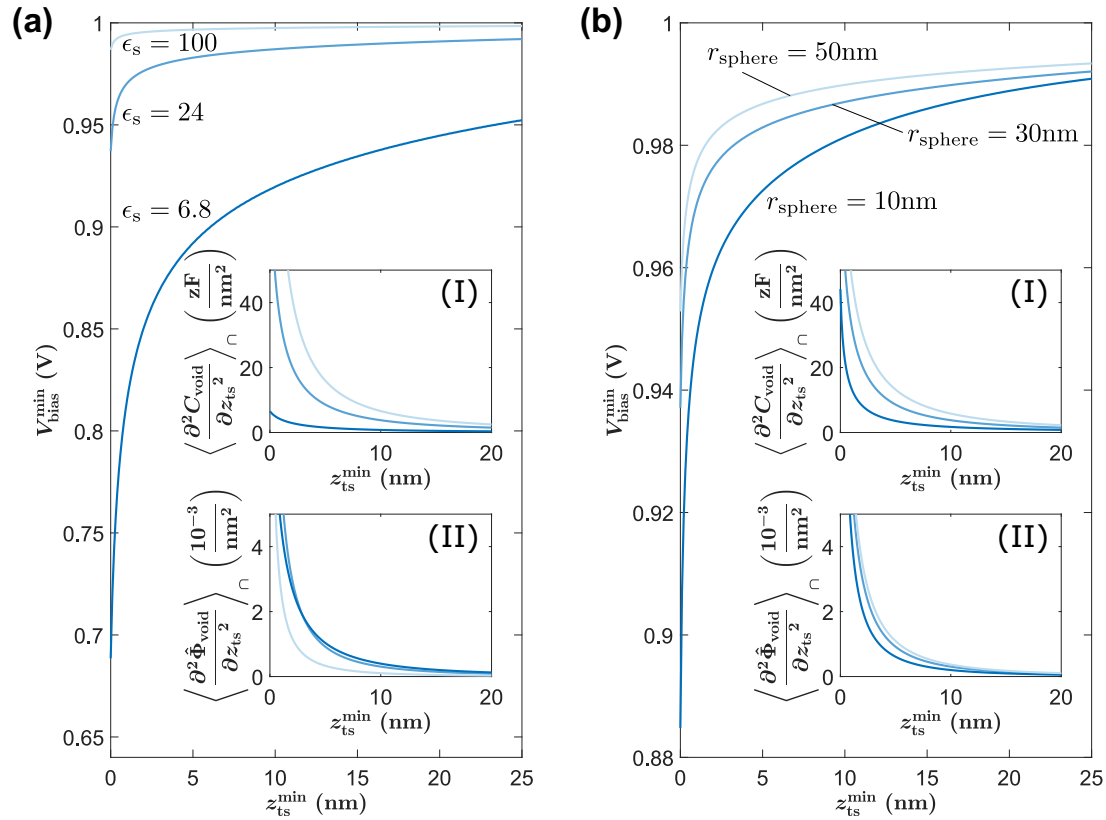

FIG. 7. Dependency of $V_{bias}^{min}(z_{ts}^{min})$ on (a) the sample permittivity ϵ_s with $r_{sphere} = 30$ nm and on (b) the sphere radius r_{sphere} with $\epsilon_s = 24$, both for the SCL model. An oscillation amplitude $A = 5$ nm, parameters from Table I, $\epsilon_s = 24$, and $V_{CPD} = 1$ V are used. One negative charge $q = -e$ is placed at $\vec{r}_0 = [0, 0, 0]$. The successive tint of the line colors represents (a) the different permittivity values ($\epsilon_s = 6.8$, 24, and 100) or (b) the different sphere radii ($r_{sphere} = 10$, 30, and 50 nm). Insets show the corresponding cap-averaged second derivatives of (I) the capacitance and (II) the normalized electrostatic potential.

account of all parameters, we find

$$\langle C_{void}\rangle_{\cap} = \langle C_{void}\rangle_{\cap}(x_{ts}, y_{ts}, z_c, \epsilon_s, \{p_{tip}\}, A), \tag{10}$$

$$\langle \hat{\Phi}_{void}\rangle_{\cap} = \langle \hat{\Phi}_{void}\rangle_{\cap}(\vec{r}_i, x_{ts}, y_{ts}, z_c, \epsilon_s, \{p_{tip}\}, A), \tag{11}$$

$$W_q(\vec{r}_i) = W_q(\vec{r}_i, x_{ts}, y_{ts}, z_c, \epsilon_s, \{p_{tip}\}, A). \tag{12}$$

For homogeneous, atomically flat surfaces, the vector $\vec{r}_{ts}$ in Eqs. (10)–(12) could be substituted by the scalar coordinate z_{ts}. However, for the general case of a structured surface, the lateral tip position has to be taken into account. Depending on the context, different parameters for the electrostatic quantities will be relevant in the following sections. To highlight the respective relevant dependency for the different cases, we refrain in the following from explicitly listing the full parameter list for the quantities in Eqs. (10)–(12), but give the relevant ones instead.

For the evaluation of the electrostatic model for the void system, we consider three model tip geometries as sketched in Fig. 2: a tip consisting of a sphere with radius r_{sphere} (denoted by S), a half-sphere with radius r_{sphere} attached to a cone with height h_{cone} and half opening angle Θ_{cone} (denoted by SC), and a half-sphere and a cone, as in the SC model, attached to a lever with area A_{lever} and thickness h_{lever} (denoted by SCL). The model tips have different sets of parameters $\{p_{tip}\}$, but all bear rotational symmetry with respect to the z axis. To maintain this symmetry, the lever in geometry SCL is modeled by a disk of radius r_{lever} with an area $A_{lever} = \pi r_{lever}^2$ chosen to be the same as the one of a typical rectangular cantilever. As the sensitivity to the cantilever size is neglectable when using FM detection [24], we do not consider the different oscillation amplitudes of the elements along the one-side clamped cantilever beam [20], but assume that the beam oscillates as one element. We apply two algorithms to numerically evaluate $\hat{\Phi}_{void}$ and C_{void}, namely, an implementation of the analytical model originally calculated by Smythe [25] for geometry S as well as the CAPSOL code [24] for geometries S, SC, and SCL. To check the consistency of our methods, we perform calculations using both the Smythe (denoted by S1) [25] and CAPSOL (denoted by S2) [24] methods for the sphere model and find perfect agreement. Note that the Smythe method assumes a dielectric half-space, while we choose 1 mm thickness of the dielectric support for calculations based on the CAPSOL code. Assuming a finite dimension for the dielectric support has negligible effect on the results as the length scale of the relevant interactions is orders of magnitudes smaller than 1 mm.

Clearly, geometry SCL is expected to resemble the experimental situation closest and, therefore, is expected to yield the best results. However, the comparative evaluation of geometries S, SC, and SCL yields insights into the relevance of the tip parameter set for the evaluation of V_{bias}^{min}. We

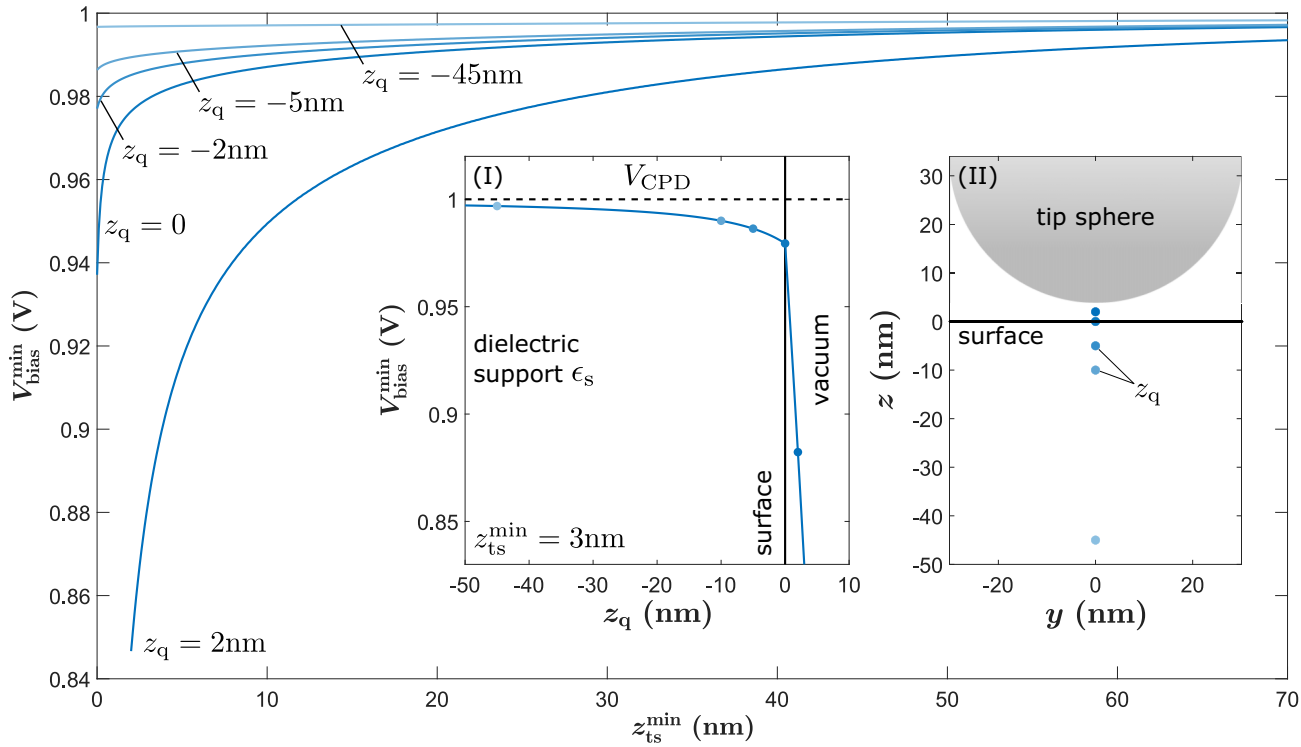

FIG. 8. V_{bias}^{min} as a function of the tip-sample distance z_{ts}^{min} for different vertical charge positions z_q of a single point charge $q = -e$ (with the elementary charge $e > 0$) located at $\vec{r} = [0, 0, z_q]$ with the tip positioned at $x_{ts} = y_{ts} = 0$. Vertical charge positions z_q are chosen in the range from -45 to 2 nm. The SCL model, an oscillation amplitude of $A = 5$ nm, tip-model parameters listed in Table I, $\epsilon_s = 24$, as well as $V_{CPD} = 1$ V are used in the simulation. Inset (I) represents V_{bias}^{min} as a function of the vertical charge position z_q at constant minimum tip height $z_{ts}^{min} = 3$ nm, while inset (II) is a sketch of the tip geometry and the charge positions.

start the exploration by performing the intermediate steps of calculating quantities $\langle \frac{\partial^2 C_{void}}{\partial z_{ts}^2} \rangle_\cap(z_c)$ and $\langle \frac{\partial^2 \hat{\Phi}_{void}}{\partial z_{ts}^2} \rangle_\cap(z_c)$ for the different models and by investigating contributions of the different tip elements to these quantities. The dimensions listed in Table I are adapted from commercially available cantilevers with metal coating that are commonly employed for KPFM experiments and are, unless otherwise noted, used for the following numerical evaluations. The results for the capacitance and electrostatic potential including their gradients and respective weighted averages along the tip oscillation path are presented in Figs. 3 and 4, respectively, for $\epsilon_s = 24$. The averages are plotted as a function of the tip oscillation center position z_c [19]. The colors correspond to the tip geometries: S in red, SC in green, and SCL in blue, while the different tint of these colors indicate the respective amplitude as depicted by the color bars in Figs. 3(d) and 4(d).

Naturally, the capacitance $C_{void}(z_{ts})$ as a function of the tip-sample distance z_{ts} is found to be a monotonically decreasing function and capacitance values of the sphere model tip (S) are several orders of magnitude smaller than those of the SC and SCL model tips [see Fig. 3(a)]. The focus here is calculating the weight functions $W_q(\vec{r}_i)$, where rather the curvature than the absolute value of the capacitance is relevant. With each step of differentiation with respect to z_{ts}, the curves for the different models come closer to each other [see Figs. 3(b) and 3(c)]. The differences are further reduced when calculating $\langle \frac{\partial^2 C_{void}}{\partial z_{ts}^2} \rangle_\cap(z_c)$ as shown in Fig. 3(d) for a series of oscillation amplitudes.

The normalized electrostatic potential $\hat{\Phi}_{void}(\vec{r}_i)$, evaluated at $\vec{r}_i = \vec{r}_0 = [0, 0, 0]$ for the tip at $\vec{r}_{ts} = [0, 0, z_{ts}]$, shown in Fig. 4 as a function of the tip-sample distance z_{ts} exhibits a decaying behavior. Here, potential values are of the same order of magnitude for the different tip models, yet, we find qualitative differences. While $\hat{\Phi}_{void}(z_{ts})$ for model S quickly decays towards zero over the shown range, the decay of the other models is much slower. However, differences between the models vanish upon differentiation. Notably, the cap-averaged second derivatives $\langle \frac{\partial^2 \hat{\Phi}_{void}}{\partial z_{ts}^2} \rangle_\cap(z_c)$ shown in Fig. 4(d) are almost identical for the different tip geometries.

To explore the situation relevant for a CFM measurement, we now assume that a charge is placed at the position $\vec{r}_i = \vec{r}_0$ and the tip oscillates along the z-axis symetrically to z_c. The weight function W_q at the position $\vec{r}_0$ as a function of z_c is calculated for models S, SC, and SCL and for amplitudes A varied in the range from 2 to 18 nm with results shown in Fig. 5. A strong dependency of W_q on the oscillation amplitude and on the tip model is apparent and further dependencies will be investigated in the following sections. These dependencies will directly translate into the CFM signal V_{bias}^{min} via Eq. (9) and it is, therefore, evident that V_{bias}^{min} values determined with different oscillation amplitudes or under otherwise different conditions cannot be compared to each other.

In summary, when calculating properties along the surface normal through the tip center, the cap-averaged capacitance gradient exhibits a more critical dependence on the tip model

than the cap-averaged electrostatic potential gradient. As modeling a realistic tip at the nanoscale is a most difficult endeavor, for the practical exploitation of the CFM method, it would be most desirable to determine $\langle \frac{\partial^2 C_{\text{void}}}{\partial z_{\text{ts}}^2} \rangle_{\cap}(z_{\text{c}})$ directly from the experiment rather from a model. Furthermore, the cap-averaged second derivatives of the electrostatic capacitance [Fig. 3(d)] and the normalized potential [Fig. 4(d)] both exhibit a strong dependency on the oscillation amplitude A, translating into a strong amplitude dependency of the CFM signal $V_{\text{bias}}^{\text{min}}$.

III. PARAMETERS DETERMINING THE CFM VOLTAGE

Now, we investigate the dependency of $V_{\text{bias}}^{\text{min}}$ on experimental and material parameters for the case of a negative charge $q = -e$ (with $e > 0$) positioned at $\vec{r}_0 = [0, 0, 0]$. In particular, the CFM voltage $V_{\text{bias}}^{\text{min}}$ is calculated as a function of the tip position along the z axis with $\vec{r}_{\text{ts}} = [0, 0, z_{\text{ts}}]$ for $\epsilon_{\text{s}} = 24$ and $V_{\text{CPD}} = 1$ V unless otherwise noted.

A. Oscillation amplitude

We start by investigating the dependency of $V_{\text{bias}}^{\text{min}}$ on the oscillation amplitude A that is varied in the range of 2 to 18 nm. $V_{\text{bias}}^{\text{min}}$ is plotted in Fig. 6 as a function of (a) the minimum tip-sample distance $z_{\text{ts}}^{\text{min}}$ for different oscillation amplitudes and (b), (c) as a function of the oscillation amplitude A at fixed minimum tip-sample distances $z_{\text{ts}}^{\text{min}} = 3$ nm and $z_{\text{ts}}^{\text{min}} = 30$ nm, respectively. The position $z_{\text{ts}}^{\text{min}} = z_{\text{c}} - A$ represents the minimum tip-sample distance during the oscillation cycle and can be chosen to be zero as W_{q} always attains a finite value at $z_{\text{ts}}^{\text{min}} = 0$.

The CFM voltage exhibits the largest deviation from V_{CPD} at very small tip-sample distances [see Fig. 6(b)], while the deviation for the sphere S is largest at large tip-sample distances [see Fig. 6(c)]. We attribute this behavior to the simplicity of the sphere tip model creating an electric field that is qualitatively different from the more realistic tip models SC and SCL. As the central result, we find a scaling of $V_{\text{bias}}^{\text{min}}$ with the oscillation amplitude A over a large range of $z_{\text{ts}}^{\text{min}}$. Consequently, the oscillation amplitude A is a critical parameter for CFM measurements and it is important to experimentally determine this parameter for CFM measurements [26–28]. All further analysis will be focused on the SCL tip model.

B. Substrate dielectric constant

Results in Fig. 7(a) highlight the influence of the substrate dielectric constant ϵ_{s} on $V_{\text{bias}}^{\text{min}}$. While keeping all other parameters constant, we vary the relative permittivity to $\epsilon_{\text{s}} = 6.8$, 24, and 100 to cover the range from insulating to almost metallic samples. As expected, $V_{\text{bias}}^{\text{min}}$ values are close to V_{CPD} for large ϵ_{s}. This corresponds to the situation of a Kelvin probe measurement on an electrical conductor, where a single charge present at the surface has only a minute effect on the work function measurement. The deviation of $V_{\text{bias}}^{\text{min}}$ from V_{CPD} is increasing with decreasing ϵ_{s} and we yield the plausible result that most sensitive charge measurements are possible on a strongly insulating substrate. This behavior is qualitatively the same for the other tip geometries as shown in Appendix A

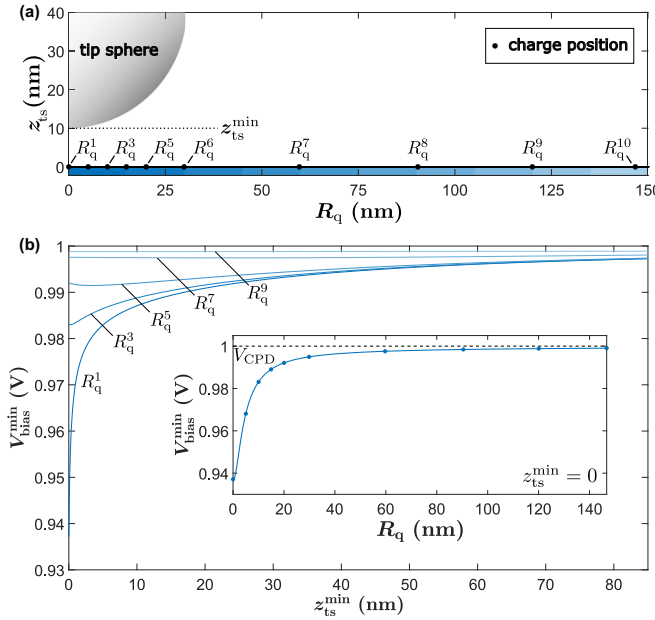

FIG. 9. Effect of the lateral charge position on $V_{\text{bias}}^{\text{min}}$. (a) Model geometry including charges at radial positions $R_{\text{q}}^i = \sqrt{(x_{\text{q},i})^2 + (y_{\text{q},i})^2}$ for $z_{\text{q}} = 0$ and the tip at position $\vec{r}_{\text{ts}} = [0, 0, z_{\text{ts}}^{\text{min}}]$. (b) $V_{\text{bias}}^{\text{min}}$ data as a function of the tip-sample distance $z_{\text{ts}}^{\text{min}}$ for single point charges $q = -e$ at selected radial positions R_{q}^i. The SCL tip model, an oscillation amplitude of $A = 5$ nm, parameters from Table I, $\epsilon_{\text{s}} = 24$, and $V_{\text{CPD}} = 1$ V are used for the simulation. The inset in (b) represents $V_{\text{bias}}^{\text{min}}$ as a function of the radial displacement R_{q} at $z_{\text{ts}}^{\text{min}} = 0$.

[Fig. 13(a)] and can be traced to an increased sensitivity of the cap-averaged second capacitance gradient to ϵ_{s} [see inset (I) in Fig. 7(a)]. As the actual ϵ_{s} of the substrate is often not well known, this finding points to the importance of an experimental determination of $\langle \frac{\partial^2 C_{\text{void}}}{\partial z_{\text{ts}}^2} \rangle_{\cap}(z_{\text{ts}})$.

C. Sphere radius

The impact of the sphere radius r_{sphere} on $V_{\text{bias}}^{\text{min}}$ is shown in Fig. 7(b). When exploring $V_{\text{bias}}^{\text{min}}$ within realistic ranges of $\{p_{\text{tip}}\}$, we find that the sphere radius is the most critical parameter of the tip geometry, while a change of cone and lever dimensions within the same order of magnitude has a significantly smaller effect (data not shown). Larger deviations of $V_{\text{bias}}^{\text{min}}$ from V_{CPD} are found for smaller sphere radii. Furthermore, a rapid decay of $V_{\text{bias}}^{\text{min}}$ with increasing $z_{\text{ts}}^{\text{min}}$ is found for large tip radii r_{sphere}, yet the absolute signal is smaller. This behavior is attributed to strong lateral averaging of a large tip [29] and the differences highlight that the tip radius is a critical parameter for charge quantification.

IV. CFM VOLTAGE AS A FUNCTION OF THE CHARGE POSITION

Aside from the system parameters, the magnitude of $V_{\text{bias}}^{\text{min}}$ has a clear dependency on the charge position relative to the lateral position $(x_{\text{ts}}, y_{\text{ts}})$ and the lower turning point $z_{\text{ts}}^{\text{min}}$ of the tip oscillation. In particular, the following analysis will highlight the nonlocal character of the CFM detection principle.

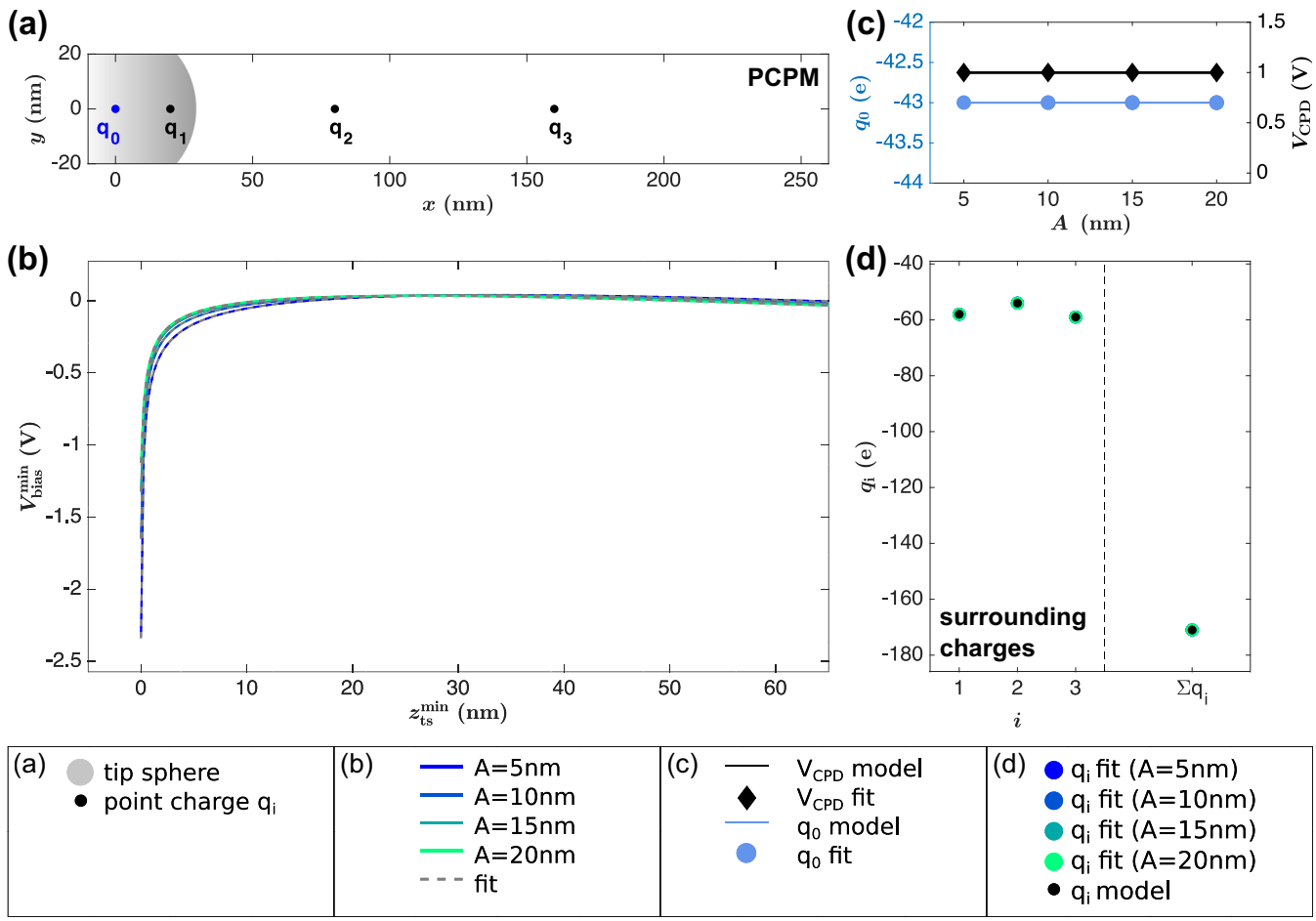

FIG. 10. Results of the optimization routine for a charge distribution with three point charges q_1, q_2, and q_3 at different distances to the central charge of interest q_0. (a) Point-charge position map (PCPM) illustrating the charge positions. (b) Artificially generated measurement data $V_{\text{bias,meas}}^{\text{min}}$ as a function of the tip-sample distance $z_{\text{ts}}^{\text{min}}$. The curves are generated for oscillation amplitudes $A = 5$ nm (dark blue), 10 nm (lighter blue), 15 nm (dark green), and 20 nm (light green) using $\epsilon_s = 24$, $V_{\text{CPD}} = 1$ V, and parameters from Table I. The $V_{\text{bias}}^{\text{min}}$ curves fitted to these data by the optimization algorithm are depicted by gray dashed lines. (c) Model and resulting values for the fit parameters q_0 and V_{CPD} as a function of the amplitude A. (d) Model and resulting values for the surrounding charges q_i ($i = 1, 2, 3$) and their sum for the different amplitudes A indicated by the same colors of the points as in (b).

A. Vertical charge position

First, the CFM signal $V_{\text{bias}}^{\text{min}}$ is investigated with respect to the tip-sample distance $z_{\text{ts}}^{\text{min}}$ for a single point charge located at different central vertical positions with results presented in Fig. 8. Vertical charge positions z_{q} in the range from -45 to 2 nm for the SCL model (see inset II in Fig. 8 for a sketch of the geometry) and an oscillation amplitude of $A = 5$ nm are chosen. The vertical position range includes the dielectric boundary and extends along the negative direction up to a vertical distance of more than the tip radius. In all cases, the $V_{\text{bias}}^{\text{min}}(z_{\text{ts}}^{\text{min}})$ curves exhibit the largest deviation from V_{CPD} at small tip-sample distances and approach V_{CPD} for large $z_{\text{ts}}^{\text{min}}$. The CFM voltage as a function of the charge position z_{q} but at a fixed tip height of $z_{\text{ts}}^{\text{min}} = 3$ nm is presented in inset (I) of Fig. 8. The slope with respect to z_{q} differs on either side of the dielectric boundary: Due to the high electric field at the tip apex, a large slope of $V_{\text{bias}}^{\text{min}}(z_{\text{ts}}^{\text{min}})$ is present in the gap between tip and dielectric. The polarization of the dielectric medium surrounding the point charge at $z_{\text{q}} < 0$ leads to a slow decay towards V_{CPD} for large z_q. A similar behavior is found for the S and SC tip models (see Appendix A, Fig. 14). This example particularly shows that charges buried inside the dielectric substrate, such as charged defects or vacancy sites, contribute to the $V_{\text{bias}}^{\text{min}}$ voltage and, therefore, can compromise the CFM measurement of charges of interest.

B. Lateral charge position

Second, the CFM signal $V_{\text{bias}}^{\text{min}}(z_{\text{ts}}^{\text{min}})$ is evaluated for different lateral point charge positions at the substrate surface ($z_{\text{q}} = 0$) with results shown in Fig. 9. Since the SCL tip model bears rotational symmetry along the z axis, any lateral charge position $(x_{\text{q}}, y_{\text{q}})$ can be mapped to one radial coordinate $R_{\text{q}} = \sqrt{x_{\text{q}}^2 + y_{\text{q}}^2}$ measured from the lateral tip position. Consequently, with a rotational symmetric tip, it is not possible to distinguish between charges present at different lateral positions of identical radial distance R_{q}. Instead, the $V_{\text{bias}}^{\text{min}}$ voltage of several charges located at the same radial distance R_{q}

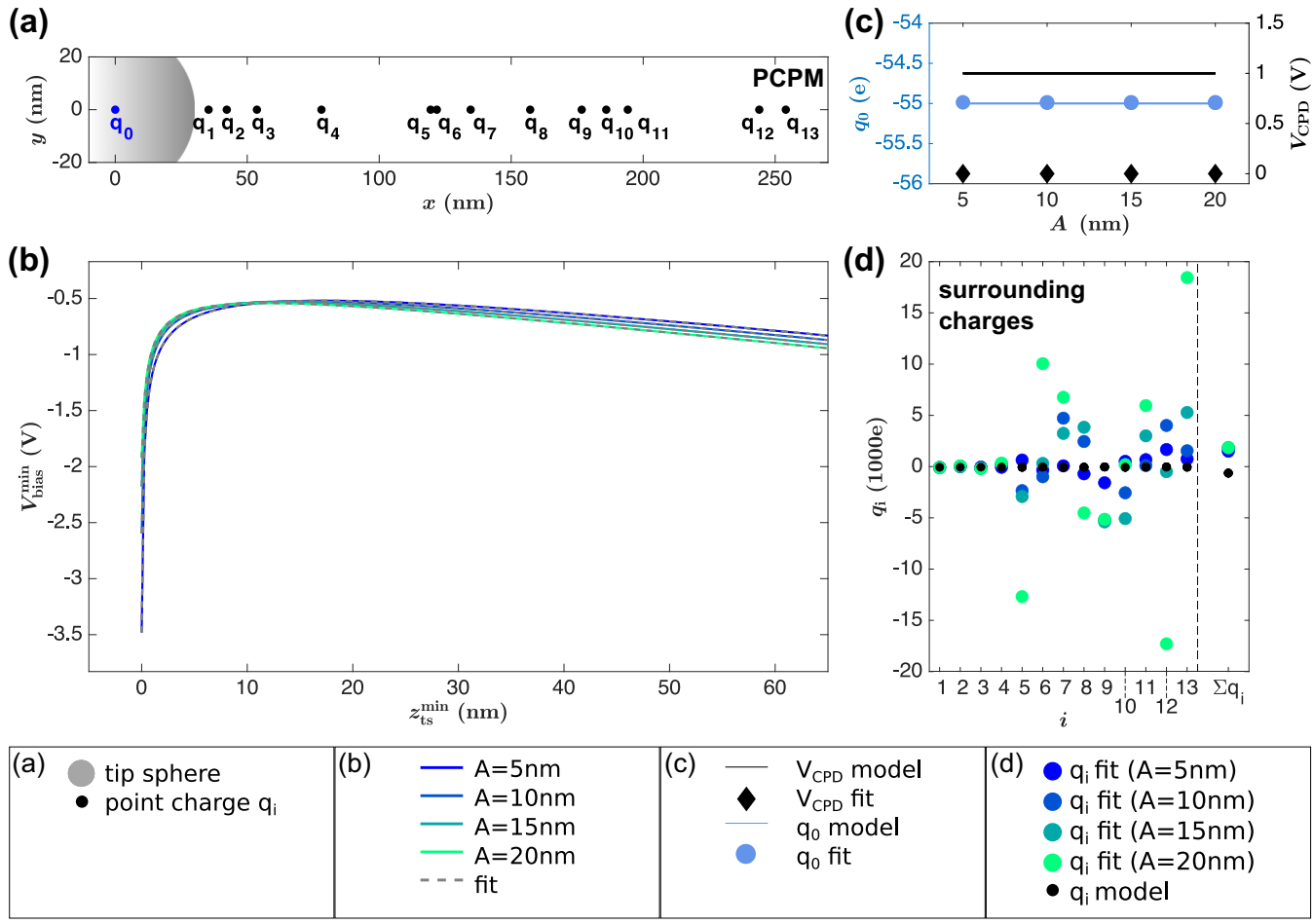

FIG. 11. Results of the optimization routine for a complex charge distribution with 13 point charges q_i surrounding a central charge of interest q_0. (a) Point-charge position map (PCPM) illustrating the charge positions. (b) $V_{bias,meas}^{min}$ data as a function of the tip-sample distance z_{ts}^{min}. The curves are generated for oscillation amplitudes $A = 5$ nm (dark blue), 10 nm (lighter blue), 15 nm (dark green), and 20 nm (light green) using $\epsilon_s = 24$, $V_{CPD} = 1$ V, and parameters from Table I. V_{bias}^{min} curves fitted to these data by the optimization algorithm are depicted by gray dashed lines. (c) Model and resulting values for the fit parameters q_0 and V_{CPD} as a function of the amplitude A. (d) Model and resulting values for the surrounding charges q_i ($i = 1, \ldots, 13$) for the different amplitudes A indicated by the same colors of the points as in (b).

are equal to the V_{bias}^{min} voltage corresponding to the sum of their charge magnitudes. We expect that the rotational symmetry is a reasonable approximation for experiments as AFM tips are usually fabricated with the aim to being rather symmetric. Figure 9(a) visualizes the tip geometry and the model charge positions on the radial axis with charges positioned within ($i = 1 \ldots 6$) and beyond ($i = 7 \ldots 10$) the xy-projected tip sphere. $V_{bias}^{min}(z_{ts}^{min})$ curves calculated for exemplary individual charges are shown in Fig. 9(b) whereby the charges are named by their radial positions R_q^i.

All curves exhibit their maximum deviation from V_{CPD} at or close to $z_{ts}^{min} = 0$. The CFM voltage at $z_{ts}^{min} = 0$ is closer to V_{CPD} for large radial charge positions. This is in agreement with a reduced sensitivity to a point charge located far away from the lateral tip position as is further highlighted by the inset in Fig. 9(b), where $V_{bias}^{min}(z_{ts}^{min} = 0)$ is plotted as a function of the radial charge position R_q.

At larger tip-sample distances, V_{bias}^{min} voltages approach V_{CPD}, however, $V_{bias}^{min}(z_{ts}^{min})$ does not converge against V_{CPD} within the investigated tip-sample distance regime. Instead, the V_{bias}^{min} voltages differ, depending on the lateral charge position, by several mV from V_{CPD} even at $z_{ts}^{min} = 80$ nm. Moreover, not all $V_{bias}^{min}(z_{ts}^{min})$ curves are strictly monotonic with respect to z_{ts}^{min}, but may exhibit an intermediate extremum [see, for example, $V_{bias}^{min}(z_{ts}^{min})$ data for R_q^5 in Fig. 9(b)]. The positions of these extrema shift towards larger z_{ts}^{min} with larger radial charge position R_q what can be explained by the form of the weight function for charges W_q, specifically by the transition in the electrostatic quantities between the sphere-dominated and the cone-influenced regimes. An intermediate extremum, and a qualitative agreement with all other observations discussed in this section, is also observed for the other tip geometries S and SC as shown in Appendix A, Fig. 15.

As expected, the strongest contribution of a point charge to V_{bias}^{min} is found for positions close to the tip apex, while the influence diminishes for positions further away. However, even charges located at radial distances of $R_q \geqslant 100$ nm contribute to the V_{bias}^{min} signal. As is apparent for R_q^7 or R_q^9 in Fig. 9(b), the contribution is rather constant with respect to the tip-sample distance z_{ts}^{min} and effectively appears as an offset to V_{bias}^{min}. Consequently, if multiple charges are present

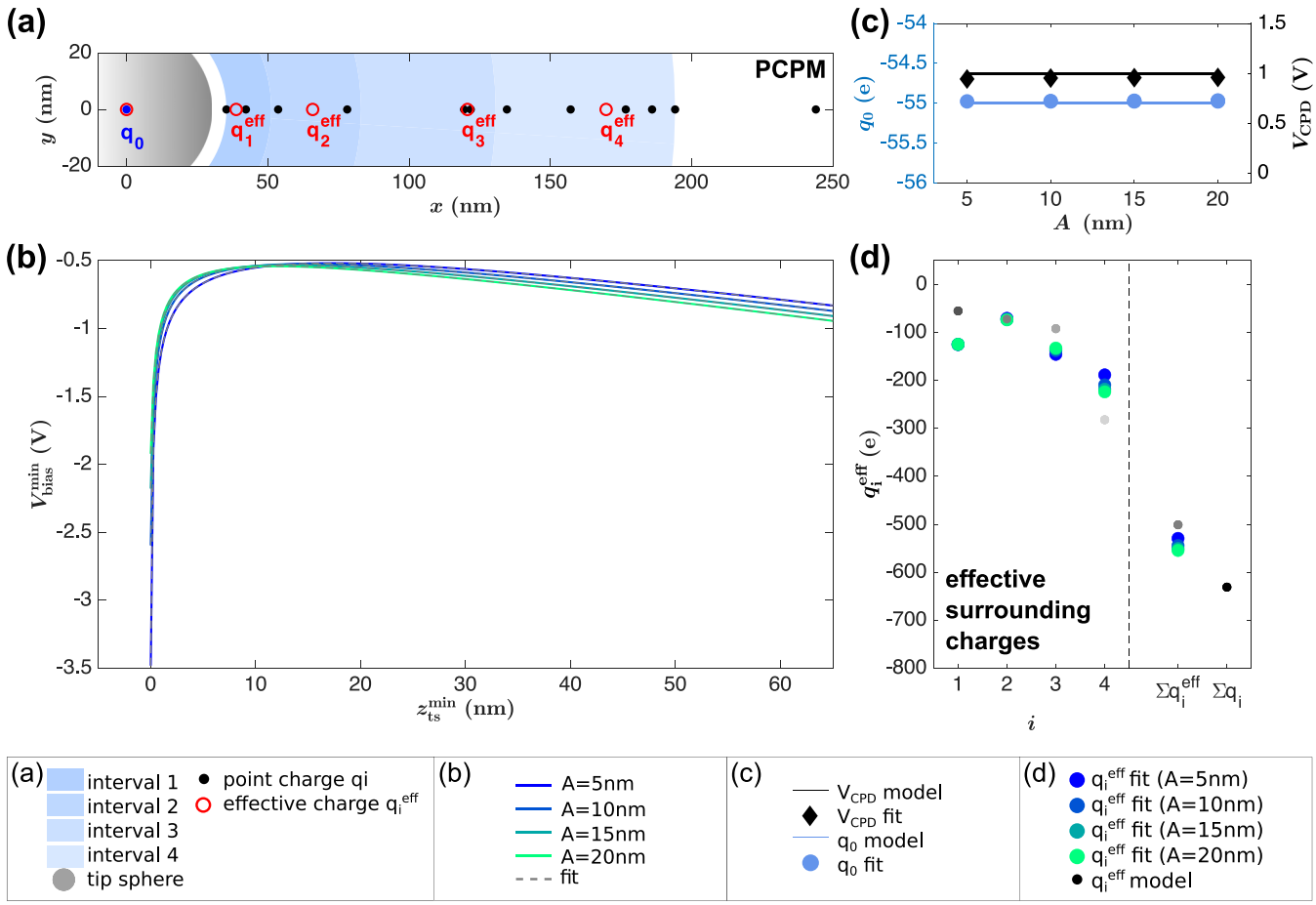

FIG. 12. Introduction of effective charges q_i^{eff} for the charge distribution in Fig. 11. (a) Point-charge position map (PCPM) showing the full charge distribution with point charges q_i (black points, identical positions, and magnitudes as in Fig. 11) used for $V_{\text{bias,meas}}^{\text{min}}(z_{\text{ts}}^{\text{min}})$ data generation as well as the effective charges q_i^{eff} (red circles) used as parameters for the fitting routine. The blue segments represent the different ranges in which the effective charges q_i^{eff} are placed. (b) $V_{\text{bias,meas}}^{\text{min}}$ data as a function of the minimum tip-sample distance $z_{\text{ts}}^{\text{min}}$. The simulation is performed for oscillation amplitudes $A = 5$ nm (dark blue), 10 nm (lighter blue), 15 nm (dark green), and 20 nm (light green) as well as for $\epsilon_s = 24$, $V_{\text{CPD}} = 1$ V, and parameters from Table I. The corresponding $V_{\text{bias}}^{\text{min}}$ curves resulting from the optimization algorithm are depicted by gray dashed lines. (c) Model and resulting values for the fit parameters q_0 and V_{CPD} as a function of the amplitude A. (d) Model and resulting values for the surrounding effective charges q_i^{eff} ($i = 1, 2, 3, 4$) and their sum for the different amplitudes A indicated by the same colors of the points as in (b).

in the system, it is likely that these have to be considered when determining the magnitude of a point charge centered underneath the tip and that their contribution can hardly be distinguished from V_{CPD}. These observations underline the necessity of performing charge quantification by distance-dependent measurements on a central charge while taking the surrounding charges into account.

V. CHARGE QUANTIFICATION

Based on the previous understanding of the CFM voltage, we introduce in this section an approach to determine the charge state of a central charge q_0 positioned at $\vec{r}_0 = [0, 0, 0]$. In particular, we demonstrate that the central charge q_0 can be retrieved with high accuracy even if a number of surrounding point charges q_i are present, a situation frequently given in experiments.

A. Optimization algorithm

The central approach for charge determination lies in the fitting of $V_{\text{bias}}^{\text{min}}(z_{\text{ts}}^{\text{min}})$ data with the charge magnitudes and the contact potential difference as free fit parameters. Here, we demonstrate the robustness of this approach by numerical simulations. Along these lines, we implement an optimization algorithm for fitting Eq. (8) to $V_{\text{bias,meas}}^{\text{min}}(z_{\text{ts}}^{\text{min}})$ data of a simulated measurement of a charge distribution with $N + 1$ point charges q_i at positions $\vec{r}_i$. The MATLAB® function `fminsearch` is used to iteratively reduce the root-mean-square (rms) difference between the measured $V_{\text{bias,meas}}^{\text{min}}(z_{\text{ts}}^{\text{min}})$ and calculated $V_{\text{bias}}^{\text{min}}(z_{\text{ts}}^{\text{min}})$ data with q_i ($i = 0 \ldots N$) and V_{CPD} as fit parameters. We consider charge distributions of different complexity and generate corresponding artificial $V_{\text{bias,meas}}^{\text{min}}(z_{\text{ts}}^{\text{min}})$ data. These data shall represent experimental situations where a nano-object like a metal cluster is charged by some or some 10 elementary charges. For testing the optimization routine, we utilize tip model S evaluated by the Smythe formulas [25].

Tip model S is chosen here to reduce computational time, yet other reasonable tip models are expected to work as well.

First, we introduce a charge distribution consisting of a central charge q_0 at $\vec{r}_0 = [0, 0, 0]$ and three surrounding charges q_1, q_2, and q_3 placed at radial positions $R_q^1 = 20\,\text{nm}$, $R_q^2 = 80\,\text{nm}$, and $R_q^3 = 160\,\text{nm}$, all at $z_q = 0$. The geometry of this distribution including the tip sphere is shown in top view in Fig. 10(a) what we further on denote as the point-charge position map (PCPM). Charge magnitudes q_i are randomly chosen in the interval between $-30e$ and $-60e$ (with the elementary charge $e > 0$). We do not see any fundamental limitation of the charge magnitude in further simulations with different charge magnitudes (see Appendix B, Fig. 16 for one example with smaller charge magnitudes). The distance-dependent data are calculated for the given charge distribution using amplitude values $A = 5$, 10, 15, and 20 nm parameters listed in Table I, $\epsilon_s = 24$, and $V_{CPD} = 1\,\text{V}$. The resulting $V_{bias,meas}^{min}(z_{ts}^{min})$ curves are depicted in Fig. 10(b). Note that for a simulation with all q_i having the same sign, the nonmonotonic behavior in the CFM data is characteristic to the S model tip and does not represent a physical property of the distribution of charges under investigation.

Second, we test the optimization routine by recovering the "unknown" charge magnitudes q_0, q_1, q_2, and q_3 as well as V_{CPD} by fitting $V_{bias}^{min}(z_{ts}^{min})$ to the data generated in the first step. Starting values are chosen for V_{CPD} as zero and for q_i as one negative elementary charge. The optimization is performed until one of the two following termination criteria is reached: (1) The optimization exceeds 5000 iterations, (2) the difference (`TolX`) in q_i/e and $V_{CPD}/\,\text{V}$ between two subsequent optimization steps is less than 10^{-6} and the change (`TolFun`) in the rms difference between $V_{bias,meas}^{min}(z_{ts}^{min})$ and $V_{bias}^{min}(z_{ts}^{min})$ is less than 1 pV for two subsequent iteration steps. For a reliable charge quantification it is necessary to reach criterion (2). The resulting $V_{bias}^{min}(z_{ts}^{min})$ curves are included in Fig. 10(b) as dashed gray lines and perfectly match the original $V_{bias,meas}^{min}(z_{ts}^{min})$ data. Correspondingly, the values for quantities q_0, q_1, q_2, and q_3 as well as V_{CPD} are retrieved with high accuracy for all amplitudes as shown in Figs. 10(c) and 10(d). Thus, for a central charge and a small number of surrounding charges, the optimization routine perfectly recovers the charge magnitudes.

B. Concept of effective charges

Much less favorable results are obtained when increasing the number of surrounding charges; in this case the optimization problem is overdetermined. We first illustrate this challenge by a model calculation for an extended charge distribution and in a second step introduce the concept of effective surrounding charges as a solution.

First, 13 point charges q_i are randomly placed in the simulation at radial distances R_q^i ranging from 25 nm to more than 230 nm, in addition to the central charge q_0. Charge magnitudes are randomly chosen between $-30e$ and $-60e$ and the corresponding PCPM is presented in Fig. 11(a). The generated $V_{bias,meas}^{min}(z_{ts}^{min})$ curve data including the $V_{bias}^{min}(z_{ts}^{min})$ fits for different amplitudes are shown in Fig. 11(b). The fits are in excellent agreement with the simulated $V_{bias}^{min}(z_{ts}^{min})$ data and the central charge q_0 is accurately determined for all oscillation amplitudes as shown in Fig. 11(c). In contrast, the quantity V_{CPD} [see Fig. 11(c)] as well as most of the surrounding charges q_i [see Fig. 11(d)] strongly deviate from the original values and the sum of surrounding charges is not reproduced correctly [see Fig. 11(d)]. These observations can be traced to the properties of the weight function for charges W_q averaging over charges in near proximity to each other and the subsequent overdetermination of the optimization problem.

A particularly illustrative example for the insensitivity of W_q to neighboring charges can be identified from charges q_5 and q_6. As both charges are placed in close proximity to each other at large R_q, their specific contribution to $V_{bias}^{min}(z_{ts}^{min})$ via their respective $W_q(\vec{r}_i)$ function is virtually indistinguishable. Consequently, the large negative charge of q_5 is counterbalanced by the large positive charge q_6 and the fit routine aborts after reaching the maximum number of allowed iterations. Furthermore, we find that the z_{ts}^{min} dependence of W_q is not significant for charges positioned at $R_q^i > 100\,\text{nm}$. In the current example, the fit routine finds a solution with charges at $R_q^i > 200\,\text{nm}$ having very large magnitudes while V_{CPD} is set to a value close to zero.

Note, however, that the magnitude of the central charge of interest is nonetheless well reproduced. This result suggests that q_0 yields the key contribution to V_{bias}^{min} with a z_{ts}^{min} dependence that is characteristic enough to provide the correct result for the central charge. Based on this finding, we seek for a stable solution yielding more realistic results for the surrounding charges. To remove surplus fit variables, we reduce the number of surrounding charges by replacing them with effective point charges. In particular, all point charges at $R_q^i > 200\,\text{nm}$ are excluded as their contribution is small and indistinguishable from V_{CPD}. The remaining point charges are subsumed into segments along the R_q axis and reduced to effective charges. Positions of these effective charges are determined as follows: The range $\Delta R_q = R_q^{max} - R_q^{min}$ is calculated from the two point charges positioned at the minimum radial distance R_q^{min} and at the maximum radial distance $R_q^{max} \leqslant 200\,\text{nm}$. Next, this range is segmented into four intervals of increasing width, namely, of $0.1\Delta R_q$, $0.2\Delta R_q$, $0.3\Delta R_q$, and $0.4\Delta R_q$. Finally, one effective point charge is placed in each of these segments at the average radial distance of point charges within the respective segment. The use of an averaged position is most reliable if the charges are of the same order of magnitude.

For the example in Fig. 11, the reduced PCPM is shown in Fig. 12(a), consisting of the central charge and four effective surrounding charges (in red). This PCPM is used to fit the $V_{bias,meas}^{min}(z_{ts}^{min})$ data calculated for the complete charge distribution. As depicted in Fig. 12(b), fit results based on the effective PCPM perfectly match the $V_{bias,meas}^{min}(z_{ts}^{min})$ curves calculated for the full PCPM. Most importantly, the central charge q_0 is determined as $-54.98\,e$ [see Fig. 12(c)], in excellent agreement with the actual value of $-55.00\,e$, while V_{CPD} is found to be 0.96 V, with a deviation of less than 5 % to the actual value of 1 V [see also Fig. 12(c)]. Due to neglecting the charges at $R_q > 200\,\text{nm}$, the latter deviation is expected. Values for the charge magnitudes q_i^{eff} are presented in Fig. 12(d), together with the values of $q_{i,model}^{eff}$ that were

calculated from the sum of all charges q_i in the corresponding interval. Both quantities are in good agreement for the inner segments, while they deviate stronger for the outer segments. This results in a slight overestimation of the sum of effective charges $\sum q_i^{\text{eff}}$ compared to the sum $\sum q_{i,\text{model}}^{\text{eff}}$. We explain these observations in particular by the effective charge q_4^{eff} and the V_{CPD} value both compensating for the omitted charges at $R_{\text{q}} > 200\,\text{nm}$. By testing different tip models and by performing cross-check calculations covering a large set of charge numbers and positions, we find that four effective charges positioned as described yield the most reliable results.

In conclusion, the introduction of effective charges to reduce the number of dependent parameters to avoid unphysical results is a robust approach for the quantification of the central charge. For the herein presented model data, the reduction of the 13 surrounding charges q_i to four effective charges q_i^{eff} as shown in Fig. 12 is found to give the best result. While less effective charges reduce the fit quality, more charges lead to the described effects of dependent fit parameters. The determination of the central charge magnitude q_0 proved to be robust in all trials, even if a single charge is located nearby the central charge for a small number of surrounding charges (see Appendix C, Fig. 17). Be aware that finding a stable solution for difficult cases can necessitate a modification of the starting parameters for the optimization routine. However, the selection does not lead to a bias in the resulting values. Instead, unphysical solutions are easily identified from comparing the results for different probe oscillation amplitudes: if the optimization algorithm is stuck in a local minimum, single outliers are present for specific amplitudes.

VI. SUMMARY AND CONCLUSIONS

The analysis in this work identifies a number of parameters that influence the absolute value of the $V_{\text{bias}}^{\text{min}}$ voltage in a charge force microscopy (CFM) experiment. It is found that the CFM voltage signal is dependent on the oscillation amplitude and the CFM technique yields best results for tips with a small radius as well as substrates with a small dielectric constant. Furthermore, the analysis confirms a substantial contribution of charges in close vicinity of the tip apex to the $V_{\text{bias}}^{\text{min}}$ signal, while the effect of charges far away from the tip apex (including charges buried inside the dielectric sample) are likely to appear as an offset to the contact potential difference in the $V_{\text{bias}}^{\text{min}}$ signal.

First and foremost, it becomes clear from this analysis that taking a *lateral* map of $V_{\text{bias}}^{\text{min}}$ is insufficient for charge quantification. Instead, the acquisition of *vertical* $V_{\text{bias}}^{\text{min}}(z_{\text{ts}}^{\text{min}})$ data is necessary for obtaining reliable CFM results. For the general case of a complex charge distribution at the surface or within a sample, charge quantification can be realized by the following four steps: First, the electrostatic model is determined, for example, by a measurement of the cap-averaged second capacitance gradient, to yield the weight function for charges. Second, the point-charge positions are identified from image data and the effective charge distribution is determined

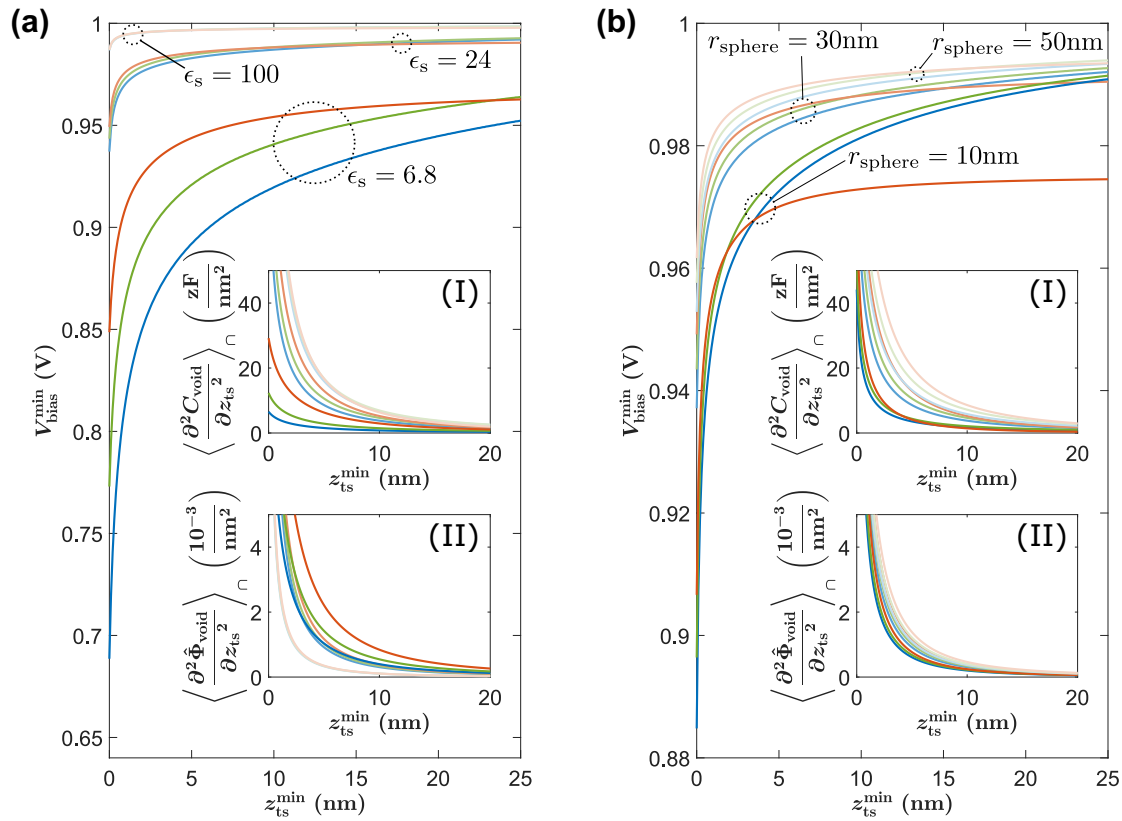

FIG. 13. Extended version of Fig. 7 highlighting the dependence of $V_{\text{bias}}^{\text{min}}$ on (a) the relative dielectric permittivity ϵ_{s} and (b) the tip radius r_{sphere}. Data for models S (SC) are presented in red (green) while data for model SCL are depicted in blue. Tinted colors are used to express the respective parameter modification. Parameters are otherwise identical to those of Fig. 7.

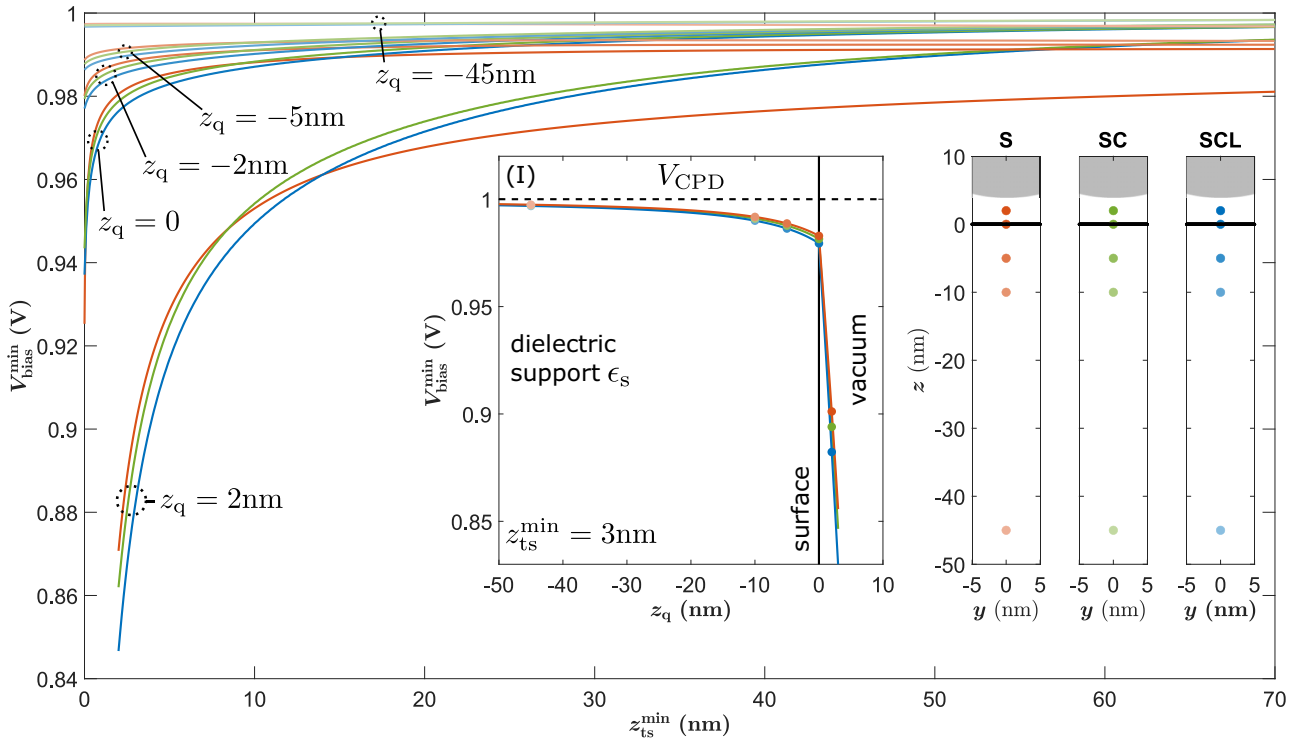

FIG. 14. Extended version of Fig. 8 highlighting the effect of the vertical charge position on V_{bias}^{min}. Data for models S (SC) are presented in red (green) while data for model SCL are depicted in blue. Tinted colors are used to express the different vertical position values. Parameters are otherwise identical to those of Fig. 8.

from these data. Third, $V_{bias}^{min}(z_{ts}^{min})$ data are systematically acquired at the position of the charge of interest for different amplitudes of the cantilever oscillation. This approach enables an inherent consistency check. Fourth, an optimization routine is used to fit V_{bias}^{min} curve data to the measurement results with the charge magnitudes q_i as well as V_{CPD} as fit parameters.

In conclusion, the CFM method holds the strong promise to offer charge quantification in numerous systems of fundamental and applied research, and by further refinement of this method, it can be expected to obtain accurate results for all relevant experimental situations.

ACKNOWLEDGMENTS

Financial support by the Deutsche Forschungsgemeinschaft via Grants No. RA2832/1-1, No. RE1186/21-1, and No. RE1186/23-1 is gratefully acknowledged. We thank C. Barth for stimulating discussions. HPC infrastructure used for the simulations is funded by the Deutsche Forschungsgemeinschaft via Grant No. 456666331.

APPENDIX A: PARAMETER ANALYSIS FOR FURTHER TIP GEOMETRIES

Simulation results for the S and SC model in addition to the SCL geometry are presented in Figs. 13–15. In particular, Fig. 13 presentes the dependency of V_{bias}^{min} on the dielectric constant of the substrace ϵ_s and on the tip sphere radius r_{sphere}. Data for only the SCL model are shown in Fig. 7 in the main text. In Fig. 14, the V_{bias}^{min} signal is evaluated for different vertical charge positions and for the S, SC, and SCL models. This figure is a generalisation of Fig. 8 in the main text. Figure 15 shows V_{bias}^{min} for different vertical charge positions, also for the S, SC, and SCL models as an extension of Fig. 9 in the main text.

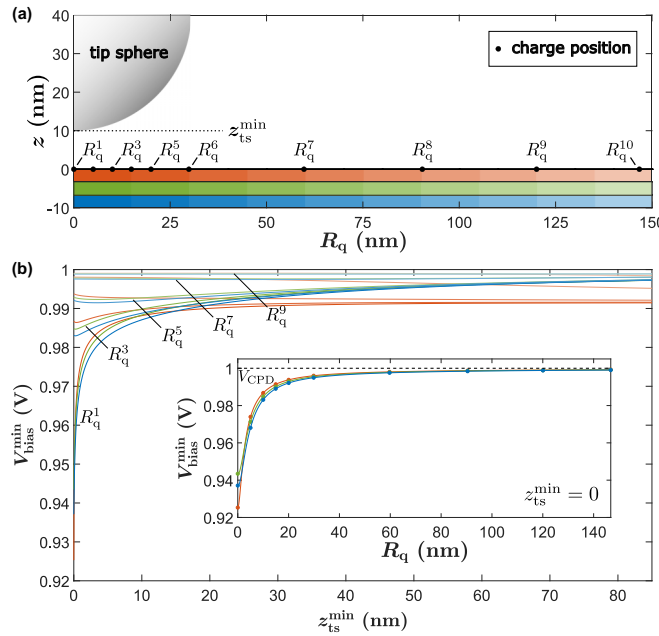

FIG. 15. Extended version of Fig. 9 highlighting the effect of the lateral charge position on V_{bias}^{min}. Data for models S (SC) are presented in red (green) while data for model SCL are depicted in blue. Tinted colors are used to express the lateral position values. Parameters are otherwise identical to those of Fig. 9.

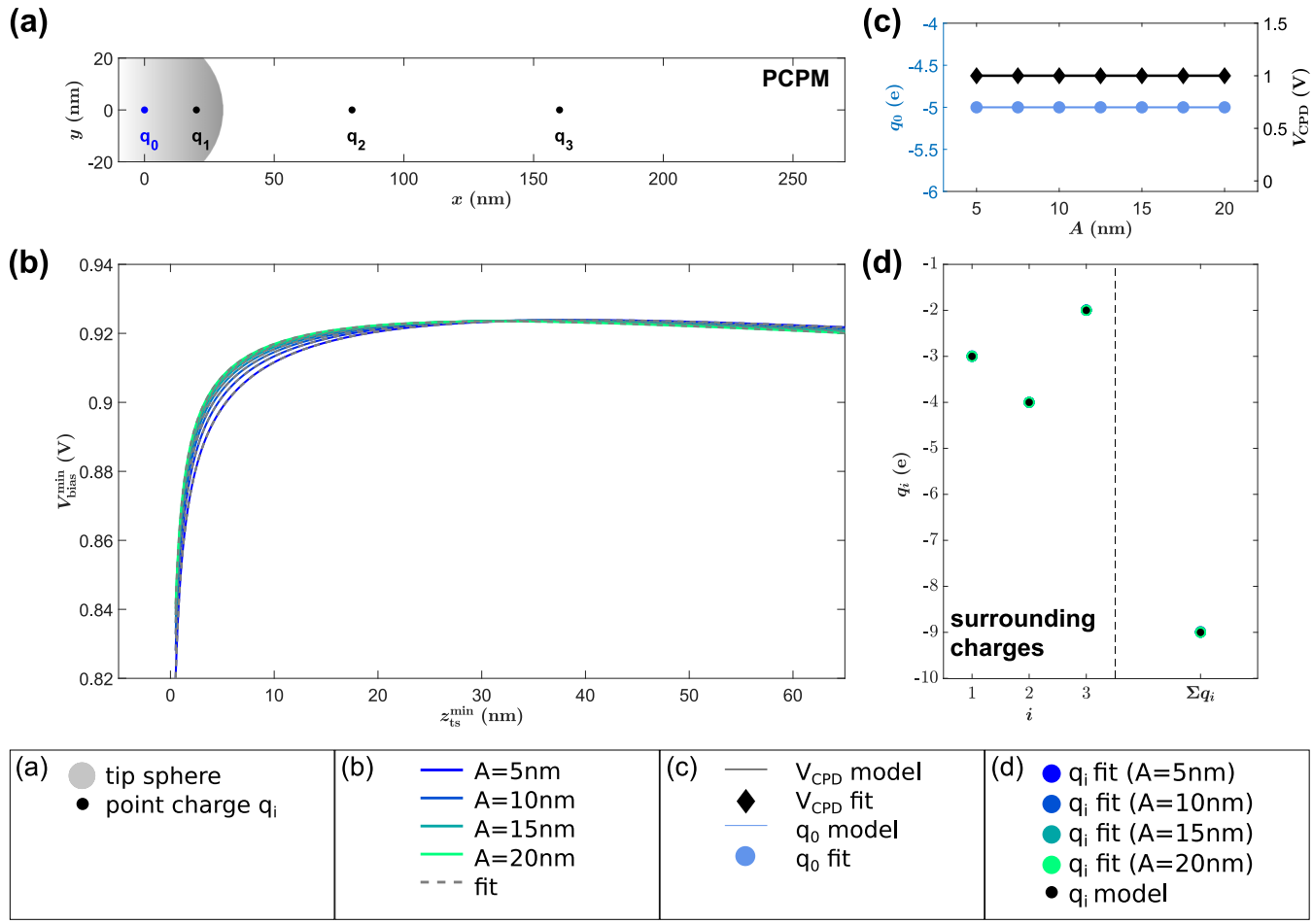

FIG. 16. Exemplary CFM experiment simulation with point charges in the range of $-1e$ to $-5e$. (a) Point-charge position map (PCPM), (b) $V_{\mathrm{bias,meas}}^{\mathrm{min}}$ data as a function of the minimum tip-sample distance $z_{\mathrm{ts}}^{\mathrm{min}}$, (c) model and resulting values for the fit parameters q_0 and V_{CPD} as a function of the amplitude A and (d) model and resulting values for the surrounding charges q_i ($i = 1, 2, 3$) and their sum as a function of the amplitude A.

APPENDIX B: SIMULATION WITH SMALL CHARGE MAGNITUDES

Figure 16 presents one example of a simulated CFM experiment with point-charge magnitudes randomly chosen in the range of $-1e$ to $-5e$. Excellent fit results are obtained.

APPENDIX C: SENSITIVITY TO NEARBY CHARGES

As shown in Fig. 17, CFM delivers excellent fit results for few charges located nearby the tip even if these charges are separated by only 2 nm.

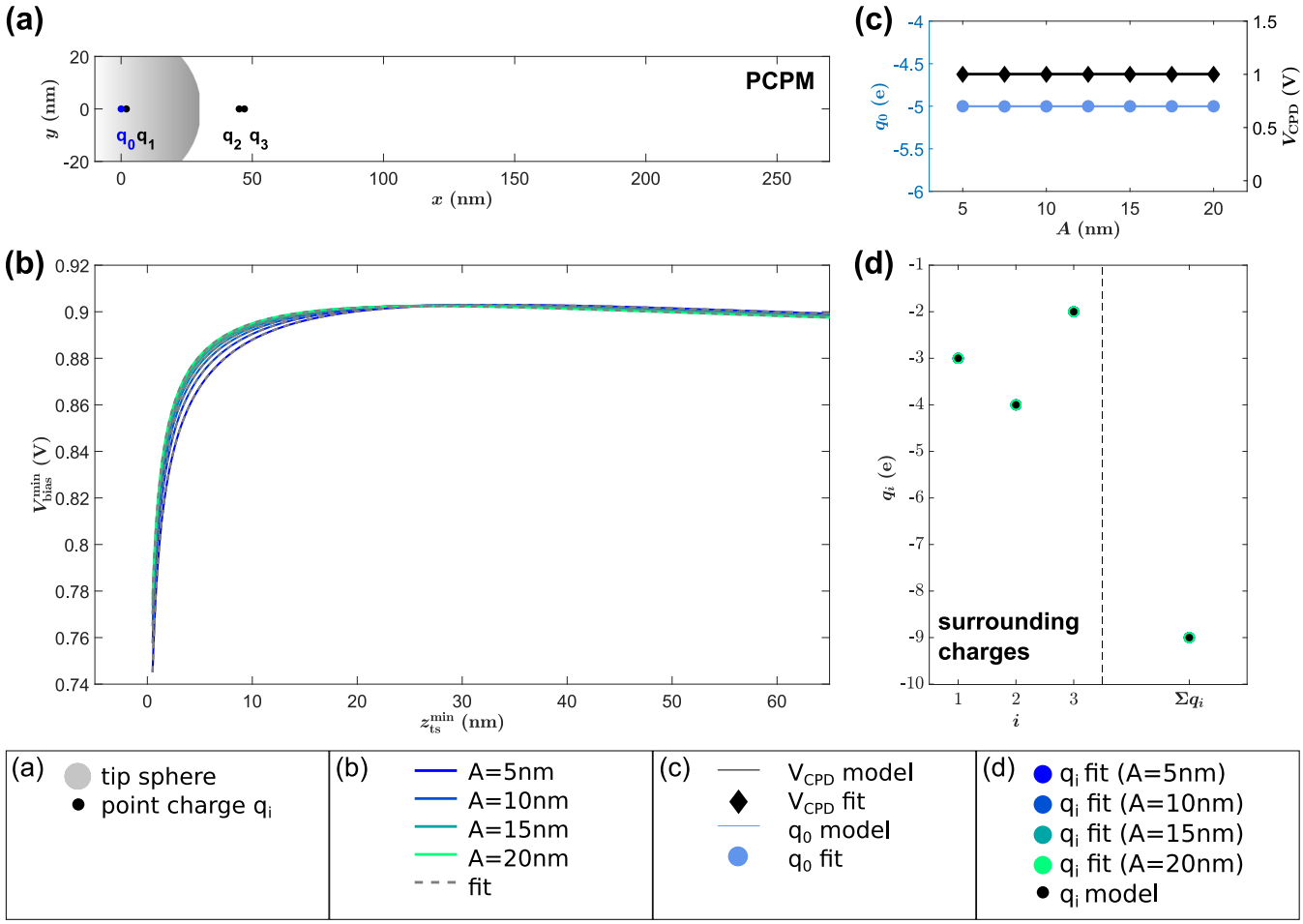

FIG. 17. Sensitivity to nearby charges. (a) Point-charge position map (PCPM), (b) $V_{\mathrm{bias,meas}}^{\mathrm{min}}$ data as a function of the minimum tip-sample distance $z_{\mathrm{ts}}^{\mathrm{min}}$, (c) model and resulting values for the fit parameters q_0 and V_{CPD} as a function of the amplitude A, (d) model and resulting values for the surrounding charges q_i ($i = 1, 2, 3$) and their sum as a function of the amplitude A.

[1] M. Mas-Torrent, C. Rovira, and J. Veciana, Surface-confined electroactive molecules for multistate charge storage information, Adv. Mater. **25**, 462 (2013).

[2] Y. Adachi, J. Brndiar, H. F. Wen, Q. Zhang, M. Miyazaki, S. Thakur, Y. Sugawara, H. Sang, Y. Li, I. Štich, and L. Kantorovich, Electron dynamics of tip-tunable oxygen species on TiO_2 surface, Commun. Mater. **2**, 71 (2021).

[3] K. Bian, W. Zheng, X. Zeng, X. Chen, R. Stöhr, A. Denisenko, S. Yang, J. Wrachtrup, and Y. Jiang, Nanoscale electric-field imaging based on a quantum sensor and its charge-state control under ambient condition, Nat. Commun. **12**, 2457 (2021).

[4] P. Rahe, R. P. Steele, and C. C. Williams, Consecutive charging of a molecule-on-insulator ensemble using single electron tunnelling methods, Nano Lett. **16**, 911 (2016).

[5] S. Fatayer, B. Schuler, W. Steurer, I. Scivetti, J. Repp, L. Gross, M. Persson, and G. Meyer, Reorganization energy upon charging a single molecule on an insulator measured by atomic force microscopy, Nat. Nanotechnol. **13**, 376 (2018).

[6] Y. Adachi, H. F. Wen, Q. Zhang, M. Miyazaki, Y. Sugawara, J. Brndiar, L. Kantorovich, I. Štich, and Y. J. Li, Charge state tristability of oxygen adatom on a rutile $TiO_2(110)$-(1×1) surface controlled by atomic force microscopy, J. Phys. Chem. C **126**, 5064 (2022).

[7] L. Gross, F. Mohn, P. Liljeroth, J. Repp, F. J. Giessibl, and G. Meyer, Measuring the charge state of an adatom with noncontact atomic force microscopy, Science **324**, 1428 (2009).

[8] F. Albrecht, J. Repp, M. Fleischmann, M. Scheer, M. Ondráček, and P. Jelínek, Probing Charges on the Atomic Scale by Means of Atomic Force Microscopy, Phys. Rev. Lett. **115**, 076101 (2015).

[9] C. Wagner, M. F. B. Green, M. Maiworm, P. Leinen, T. Esat, N. Ferri, N. Friedrich, R. Findeisen, A. Tkatchenko, R. Temirov, and F. S. Tautz, Quantitative imaging of electric surface potentials with single-atom sensitivity, Nat. Mater. **18**, 853 (2019).

[10] F. Mohn, L. Gross, N. Moll, and G. Meyer, Imaging the charge distribution within a single molecule, Nat. Nanotechnol. **7**, 227 (2012).

[11] J. F. Gonzalez, A. M. Somoza, and E. Palacios-Lidón, Charge distribution from SKPM images, Phys. Chem. Chem. Phys. **19**, 27299 (2017).
[12] L. Kelvin, Contact electricity of metals, Philos. Mag. Ser. 5 **46**, 82 (1898).
[13] W. A. Zisman, A new method of measuring contact potential differences in metals, Rev. Sci. Instrum. **3**, 367 (1932).
[14] M. Nonnenmacher, M. P. O'Boyle, and H. K. Wickramasinghe, Kelvin probe force microscopy, Appl. Phys. Lett. **58**, 2921 (1991).
[15] W. Melitz, J. Shen, A. C. Kummel, and S. Lee, Kelvin probe force microscopy and its application, Surf. Sci. Rep. **66**, 1 (2011).
[16] K. Wandelt, The local work function: Concept and implications, Appl. Surf. Sci. **111**, 1 (1997).
[17] J. L. Neff and P. Rahe, Insights into Kelvin probe force microscopy data of insulator-supported molecules, Phys. Rev. B **91**, 085424 (2015).
[18] H. Söngen, P. Rahe, J. L. Neff, R. Bechstein, J. Ritala, A. S. Foster, and A. Kühnle, The weight function for charges - a rigorous theoretical concept for Kelvin probe force microscopy, J. Appl. Phys. **119**, 025304 (2016).
[19] P. Rahe, D. Heile, R. Olbrich, and M. Reichling, Quantitative dynamic force microscopy with inclined tip oscillation, Beilstein J. Nanotechnol. **13**, 610 (2022).
[20] E. Bonaccurso, F. Schönfeld, and H.-J. Butt, Electrostatic forces acting on tip and cantilever in atomic force microscopy, Phys. Rev. B **74**, 085413 (2006).
[21] L. N. Kantorovich, A. I. Livshits, and M. Stoneham, Electrostatic energy calculation for the interpretation of scanning probe microscopy experiments, J. Phys.: Condens. Matter **12**, 795 (2000).
[22] P. Rahe and H. Söngen, Imaging static charge distributions: A comprehensive KPFM theory, in *Kelvin Probe Force Microscopy: From Single Charge Detection to Device Characterization*, edited by S. Sadewasser and T. Glatzel (Springer, Cham, 2018), pp. 147–170.
[23] H. Söngen, R. Bechstein, and A. Kühnle, Quantitative atomic force microscopy, J. Phys.: Condens. Matter **29**, 274001 (2017).
[24] A. Sadeghi, A. Baratoff, S. A. Ghasemi, S. Goedecker, T. Glatzel, S. Kawai, and E. Meyer, Multiscale approach for simulations of Kelvin probe force microscopy with atomic resolution, Phys. Rev. B **86**, 075407 (2012).
[25] W. R. Smythe, *Static and Dynamic Electricity* (Taylor & Francis, London, 1989).
[26] D. Heile, R. Olbrich, M. Reichling, and P. Rahe, Alignment method for the accurate and precise quantification of tip-surface forces, Phys. Rev. B **103**, 075409 (2021).
[27] Y. Sugimoto, Y. Nakajima, D. Sawada, K. Morita, M. Abe, and S. Morita, Simultaneous AFM and STM measurements on the Si(111)-(7 × 7) surface, Phys. Rev. B **81**, 245322 (2010).
[28] G. H. Simon, M. Heyde, and H.-P. Rust, Recipes for cantilever parameter determination in dynamic force spectroscopy: Spring constant and amplitude, Nanotechnology **18**, 255503 (2007).
[29] T. Glatzel, L. Zimmerli, S. Koch, B. Such, S. Kawai, and E. Meyer, Determination of effective tip geometries in Kelvin probe force microscopy on thin insulating films on metals, Nanotechnology **20**, 264016 (2009).